Advanced Steel Construction – Vol. 22 No. 1 (2026) 17–36
DOI:10.18057/IJASC.2026.22.1.3

SEISMIC PERFORMANCE ANALYSIS OF THE INTEGRATED MODEL FOR LARGE STADIUM STEEL STRUCTURE CANOPY

Chen-Xiao Zhang [1, 2], Chun-Jie Yu [1], Ren-Cai Jin [2], Cong-Ying Gan [1], Dong-Yun Jia [1], Foysal Bin Shakil [1] and Song Jin [1, *]

[1] *College of Architecture and Engineering, Anhui University of Technology, Maanshan 243002, China*
[2] *Technology Center, China MCC17 group Co. Ltd., Maanshan 243000, China*
** (Corresponding author: E-mail: jinsong_342601@163.com)*

ABSTRACT

Traditional seismic design method of steel canopy structures usually assumes that the lower support structure to be rigid. However, in practical engineering, the steel canopy and the lower support structure interact as an integrated system. With the innovation in design method of steel canopy structures, the seismic design of traditional large cantilever steel structure faces higher requirements. In this study, the integrated model of a large stadium steel canopy and its lower support structure is used as a reference. To consider the influence of the lower support structure, two simplified preliminary analysis models are established separately. Time history analysis is performed on all three models to evaluate simplified calculation methods for the lower support structure under seismic excitation. A series of studies are conducted to identify the causes of the discrepancies in the dynamic response among models. The study examines the effects of stiffness in-homogeneity in the lower support structure, revealing significant directional variations in stiffness across three axes. Furthermore, by analyzing peak acceleration and frequency variations between input and output for ground motion in the lower support structure, the results demonstrate that the structure's amplification and filtering effects of the lower support structure on ground motion are key contributors to in dynamic response variability. Results indicated that the seismic performance of large cantilever steel canopy structures should be evaluated using an integrated model to ensure more reliable seismic design outcomes.

ARTICLE HISTORY

Received: 27 December 2024
Revised: 24 June 2025
Accepted: 26 June 2025

KEYWORDS

Large cantilever steel canopy structures;
Seismic performance;
Lower support structure;
Ground motion;
Integrated model

1. Introduction

China is located within the seismically active zone between the Pacific Rim Seismic Belt and the Eurasian Seismic Belt, where the frequent occurrence of shallow-source earthquakes often results in severe earthquake disasters. Recent earthquake damage investigations reveal that steel canopy structures in stadiums constitute a vulnerable part in seismic design [1]. In addition to its primary functional role, the large-span spatial steel structure typically serves as a post-earthquake temporary rescue command center or aid station. Therefore, the seismic performance requirements for the spatial structure differ from those of ordinary residential buildings, necessitating compliance with region-specific seismic design codes [2]. Zhang [3, 4] and Liang [5] conducted a time-history analysis of a large-span spatial structure, studying the dynamic response and internal force distribution of the model. Lu [6] investigated the seismic performance and seismic response of large-span string trusses under rare earthquakes. The results indicate that the large-span string truss structure exhibits good seismic performance under rare earthquakes, but the weak areas of the structure still exist. Xiao [7] et al. conducted the whole process of stability analysis and the static elasto-plastic analysis under rare earthquakes on the spatial grids of an exhibition hall with vertical force transmission, indicating that the inter-story drift is minimal under multiple and rare earthquakes, and the structure's resistant lateral rigidity is substantial. Tong [8] analyzed the seismic performance and ultimate bearing capacity of three special-shaped multi-towers connected high-rise structures, quantifying the degradation patterns of both bearing capacity and stiffness under varying seismic intensities. Wang [9] proposed a new direction-dependent evolution lag coherence model for the seismic ground motions in non-stationary horizontal space. Jian [10] et al. compared the seismic responses of adjacent bridges with and without control systems, identifying critical parameters governing spatially varying ground motion effects. Rodda [11] et al demonstrated that spatial variations in vertical ground motion could significantly influence the dynamic response of large-span structures (e.g., bridges and pipelines). Bi [12] et al. quantified the structural effects of spatial ground motion variations by decomposing responses into dynamic, quasi-static, and total components. Hao [13] et al. investigated the behavior of symmetrical buildings under spatially varying base excitation and discussed the adequacy of seismic code provisions for accidental eccentricity.

Ground motions are random and dispersive, and the selection of ground motions affects the dynamic response results when using time history analysis to analyze the seismic performance of structures. Therefore, the rational selection of ground motion is imperative. Watson-Lamprey [14] et al. proposed a time series selection method for nonlinear analysis to obtain the average response of a nonlinear system rather than based on amplitude, period, and type of response spectrum. Katsanos [15] et al. demonstrated that the current seismic code framework is overly simplistic and emphasized significant inherent uncertainties in ground motion selection. Ao [16] et al. established the efficacy of multivariate regression-based selection for seismic risk assessment. Bradley [17] developed an algorithm integrating recorded and simulated motions for response history analysis. Wang[18] introduced a new algorithm for selecting and modifying ground motions, which exhibited high computational efficiency and demonstrates significant potential in enhancing seismic performance in nonlinear civil systems. Sinković [19] et al. investigated the effect that the type of target response spectrum and the number of ground motions have on the response of buildings, which indicating that these two influences were limited. For probabilistic seismic hazard analysis, Kowsari [20] et al. proposed a deviation information criterion to select the most suitable ground motion. Eftekhari [21] et al. validated data envelopment analysis (DEA) for evaluating ground motion prediction equation efficiency in site-specific studies. Gao [22] et al. demonstrated that fuzzy optimization theory can be used for the selection of ground motion recordings in structural dynamic analysis.

The support structure has a significant influence on the seismic performance of large-span spatial steel structures. Typically composed of a steel structure and a composite or concrete structure, these systems are commonly designed using decoupled models. However, integrated analysis more realistically captures their synergistic behavior. Junwu Dai's comparative analysis between simulated damage and field observations of [23] double-story mesh shell for a large-span stadium indicated that the dynamic amplification effect of the lower frame exacerbate damage to the upper grid. This underscores the necessity of employing coupled models for seismic analysis of spatial structures with concrete supports. Xue [24] systematically reviewed damping ratio determination methods and outlined future research directions for integrated systems. Nie [25-27] et al. investigated the effect of lower support structures on the seismic performance of the overall structure, which indicated that the coupling effect between the lower support structure and the single-layer cylindrical reticulated shell reduces the natural vibration frequency of the structure and significantly compromises the overall stiffness of the structure. Wang [28] introduced a simplified calculation method for the stiffness of supported structures. The comparison of the three calculation methods in terms of period, vibration pattern, and unit stresses revealed that the concrete support adversely affects the integrated model performance of the large-span space latticed structure model, which confirming the imperative for unified modeling. Yu [29] et al. analyzed two typical damage modes of steel reticulated dome structures with lower support structures to propose a failure criterion for the ultimate load-carrying capacity of a single-story steel reticulated dome's structure. The hybrid frame simulations done by Zheng [30] et al. identified maximum inter-story drifts predominantly in the lower support structure during frequent earthquakes, shifting to the upper structures under rare earthquakes. Meng [31] quantified discrepancies in portal frame analysis: decoupled models overestimated mid-span displacements and member stress ratios by 15-22% versus integrated benchmarks. Xia [32]

developed a MATLAB-based integrated modeling platform demonstrating optimal inter-story drift control and post-seismic recoverability in staggered-truss high-rises. Han [33] et al. established foundational principles for seismic design by investigating errors induced by neglecting lower support interactions in large-span reticulated domes.

In summary, conventional seismic analysis of steel canopy structures exhibits critical safety limitations due to the neglect of substructure interactions. While integrated modeling (coupling upper steel canopy with lower concrete supports) provides higher fidelity, its prohibitive computational cost and lack of established design precedents necessitate alternative approaches. This study therefore systematically investigates the seismic performance and global stability of large-span stadium canopies, with the dual objectives of developing rational simplified analytical models and establishing specialized assessment methodologies.

The case study focuses on a central stadium featuring a saddle-shaped steel canopy, shown in Fig. 1, comprising large-span spatial tube trusses with composed of ring truss, radial truss, tension cable, and facade structure. In this paper, the integrated analysis model (upper steel structure coupled with lower concrete support structure) and two simplified analysis models (separation of the upper steel structure from the lower concrete support structure) are established. By comparing and analyzing the seismic responses of the three models, a simplified method for seismic calculation for steel canopy structures is explored, which provides a reference for the preliminary design of the structure. The three-direction stiffness of the lower support structure as well as the peak and frequency changes caused by ground motion are calculated in this study. The effects of stiffness inhomogeneity for the lower support structure as well as the amplification and filtering effects of ground motion acceleration on the dynamic response of the three models are analyzed.

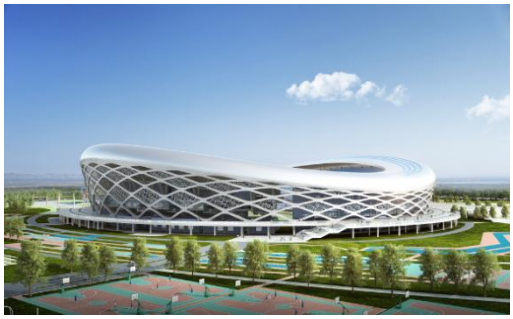

(a) Exterior of steel canopy structure stadium

(b) Interior of steel canopy structure stadium

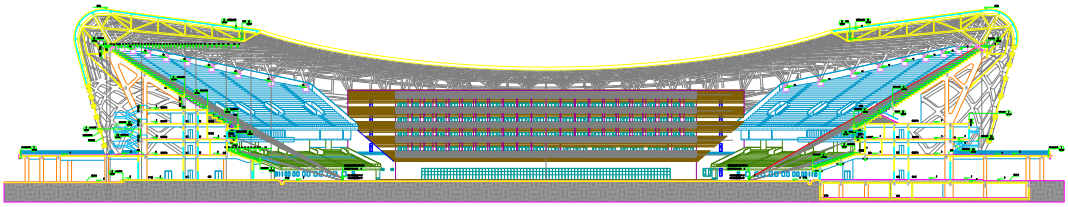

(c) East-west sectional view

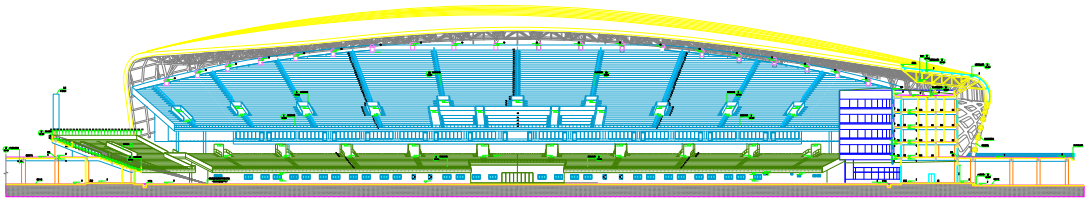

(d) North-south sectional view

Fig. 1 Steel canopy structure stadium architectural drawing

2. Model building, modal analysis and ground motion selection

2.1. Modeling of three calculations

In conventional seismic design of steel canopy structures, the lower support structure is typically idealized as rigid with perfect coupling to the steel canopy structure. To investigate dynamic characteristics of the steel canopy structure and interaction effects between the upper and lower structures, three finite element models were established using ANSYS APDL. First, separate models of the steel canopy (large-span cantilevered space-truss system) and the lower diagonally braced concrete combined trusses were developed. Subsequently, the top of each truss of the lower structure is coupled with the upper pipe truss support to shape the integrated model. Integrated model A, considering the coupling of the lower support structure with the steel canopy structure, is shown in Fig. 2(a) and Model B is a simplified separated model of the steel canopy structure, assuming that the lower support structure is rigid, as shown in Fig. 2(b). The average ground motion response of the lower support columns is applied to the upper steel canopy structure. Model C of the simplified lower support structure is created, as shown in Fig. 2(c). Models B and C are simplified computational models with lower computational costs.

The selection of Models B and C as simplified decoupled approaches is justified by three key rationales aligned with engineering practice and computational efficiency:

1. Model B: Canopy isolated analysis model (high-efficiency focus on the upper steel structure)

a) Objectives and advantages

The core purpose of this model is to isolate and evaluate the seismic response characteristics of the steel canopy, significantly reducing computational costs. It entirely ignores the dynamic calculations of the lower support structure, treating it as an infinite rigid body, and applies site ground motions only to the supports of the upper canopy.

b) Theoretical foundations

Based on the rigid base input hypothesis and static condensation method [34], its validity requires that the lower support structure has higher stiffness than the upper canopy or its dominant frequencies are far from those of the canopy (confirmability via preliminary integrated modal analysis, as shown in Fig. 5).

c) Engineering practices

This model is widely adopted in preliminary design and optimization phases of large stadium structures [35-38], as well as for rapid special performance evaluations of key components or nodes [39]. It allows engineers to efficiently focus on the canopy's performance under limited computational resources or clarifying its inherent response characteristics by parametric studies—though its natural frequencies may deviate from those of the integrated model.

2. Model C: Synergistic effect analysis model (balancing computational efficiency and interaction between the canopy and the lower support structure)

a) Objectives and advantages

This model assesses the influence of lower support structure flexibility and its dynamic response to ground motions on seismic force transfer to the steel canopy structure, while maintaining computational efficiency. It simulates the main dynamic response characteristics by significantly simplifying the lower

support structure complexity (e.g., using equivalent lumped masses, simplified beam-column models, or condensation models), taking key node values (e.g., average displacements or accelerations at all support column tops) as inputs for the upper canopy.

b) Theoretical foundations

Adopting model condensation techniques such as the Guyan condensation method, dynamic condensation method [40], establishing simple equivalent single-degree-of-freedom (SDOF) or multi-degree-of-freedom (MDOF) systems to capture the lower support structure's main dynamic characteristics in transmitting ground motions. The use of average response inputs relies on the transfer function consistency approximation under uniform support conditions [41].

c) Engineering practices

When preliminary evaluation of lower support flexibility is required but integrated modeling proves computationally prohibitive, this simplified model serves as an engineering-accepted compromise [42]. It is particularly suitable for large-scale seismic scheme screening, parametric sensitivity studies (e.g., the impact of column stiffness changes on canopy response), or rapid analysis under specific load combinations. Compared to Model B, it more reasonably reflects key dynamic interaction effects between the upper and lower structures, supporting mid-design adjustments and optimizations for canopy components sensitive to synergistic effects while significantly enhancing computational efficiency.

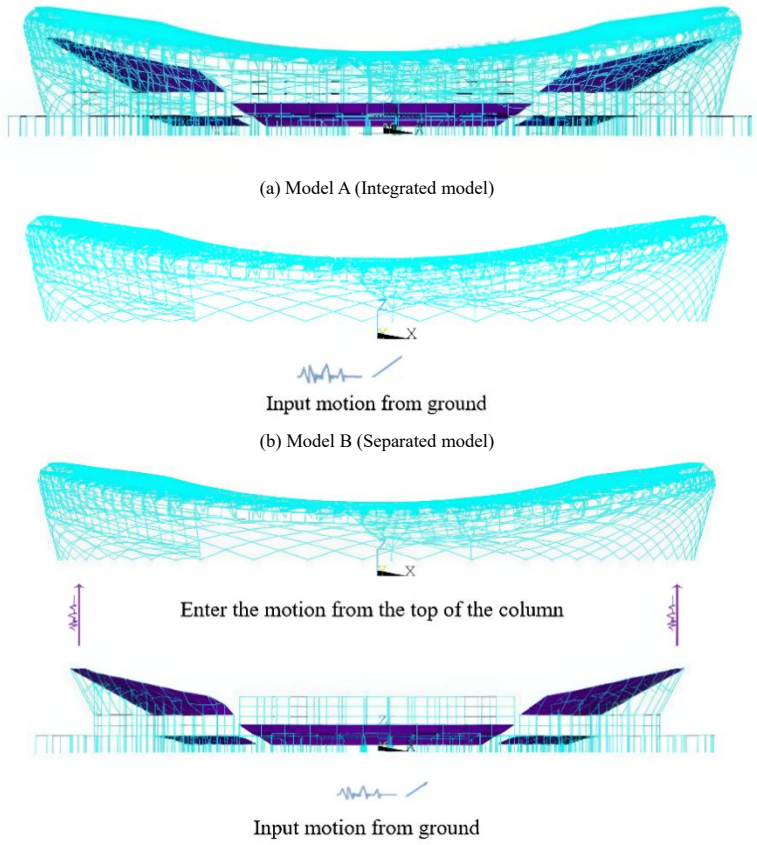

(a) Model A (Integrated model)

(b) Model B (Separated model)

(c) Model C (Separated model)

Fig. 2 Three finite element analysis models for steel canopies

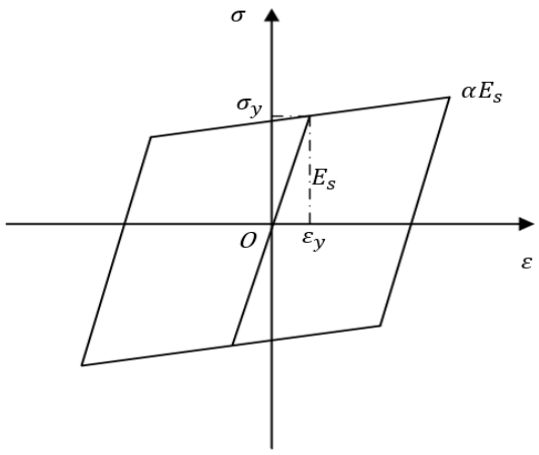

Fig. 3 Steel constitutive model

The constitutive model of steel in the finite element is in accordance with Eq. 1, and the simplified form of the model is shown in Fig. 3.

$$\sigma_s = \begin{cases} E_y \cdot \varepsilon_s & \varepsilon_s \le \varepsilon_y \\ E_y \cdot \varepsilon_y + 0.01E_y \cdot (\varepsilon_s - \varepsilon_y) & \varepsilon_s > \varepsilon_y \end{cases} \quad (1)$$

where σ_s is the stress of steel, ε_s is the strain of steel, ε_y is the yield strain of steel, E_y is the elastic modulus of steel.

The bi-linear constitutive model (Equation 1) adopted in this study assumes a post-yield stiffness ratio of 0.01, with this simplification supported by the following engineering rationales and code-compliant justifications:

1. Rationales for simplification

a) Code compatibility

Mainstream seismic design codes [43-44] require that structural systems form plastic energy dissipation mechanisms under severe earthquakes. A post-yield stiffness ratio of 0.01 accurately simulates the quasi-ideal plastic behavior of steel during the yield plateau, complying with code-specified simplifications for plastic hinge characterization.

b) Computational efficiency

For nonlinear time-history analyses of large spatial steel canopies, the bilinear model mitigates convergence issues inherent in complex hardening models (e.g., Chaboche's law), significantly enhancing analytical feasibility [45].

2. Limitations under large deformations and mitigation measures

a) Sources of potential errors

When components enter large-strain regimes, the strain-hardening behavior of actual steel may lead to an underestimation of bearing capacity by the simplified model [46]. However, this impact is offset by other safety provisions.

b) System redundancy compensation

The cross-grid structure of the canopy exhibits an internal force redistribution capacity, ensuring that local overestimation of plastic deformation do not lead to structural failure [43].

2.2. Modal analysis of steel canopy

The modal analysis is used to obtain the results of the structure's intrinsic frequency, period, vibration shapes of each mode, and the mass of participation corresponding to each vibration shape. Provide a reference for subsequent time history analysis. The proper definition of damping in a structure's dynamic analysis is critical to the accuracy of the computational results. In this study, Rayleigh damping is used.

In Rayleigh damping, assuming that the damping matrix is linear in the stiffness matrix and the mass matrix, the Rayleigh damping can be expressed as:

$$C = \alpha M + \beta K \tag{2}$$

Where C is the damping matrix, M is the mass matrix, and K is the stiffness matrix. The relationship between α and β in Rayleigh damping is:

$$\begin{Bmatrix}\alpha\\ \beta\end{Bmatrix} = \frac{2\omega_m\omega_n}{\omega_n^2-\omega_m^2}\begin{bmatrix}\omega_n & -\omega_m\\ -\frac{1}{\omega_n} & \frac{1}{\omega_m}\end{bmatrix}\begin{bmatrix}\xi_m\\ \xi_n\end{bmatrix} \tag{3}$$

ω_m , ω_n are the circular frequencies (*rad/s*) of *m*th and *n*th modes, respectively; α is the mass-proportional damping coefficient; β is the stiffness-proportional damping coefficient. The critical damping ratio is ξ.

(1) Modal analysis of separated steel canopy

The *Lanczos* algorithm was used for the modal analysis of the structure. Since the proportion of mass participation coefficients is concentrated within the top 20 modes, Table 1 presents the self-vibration frequencies, periods, and mass participation coefficients for these dominant modes.

Table 1
Modal information of separated steel canopy

Number of stages	Frequency（Hz）	Periods（s）	Mass participation factor（%）
1	1.33	0.75	19.84
2	1.45	0.69	0.19
3	1.55	0.65	1.28
4	1.73	0.58	21.34
5	1.77	0.56	4.29
6	1.87	0.53	0.93
7	2.06	0.49	8.63
8	2.15	0.47	0.04
9	2.29	0.44	0.01
10	2.36	0.42	2.92
11	2.66	0.38	1.22
12	2.67	0.37	1.45
13	3.15	0.32	0.33
14	3.19	0.31	0.37
15	3.44	0.29	0.56
16	3.52	0.28	0.30
17	3.56	0.28	0.20
18	3.58	0.28	2.07
19	3.71	0.27	0.01
20	3.77	0.27	0.56

From Table 1, it can be seen that the principal mode of vibration of the structure is concentrated in the first 8 modes, with a mass fraction proportion of 85%.

Therefore, the top 8 modes of structural self-vibration mode diagrams are taken and analyzed as shown in Fig. 4.

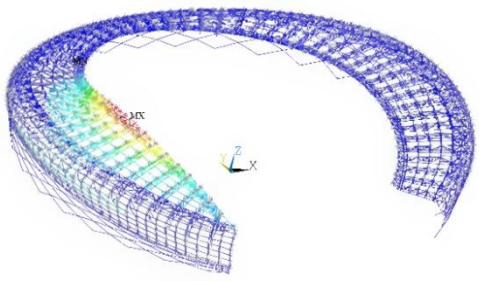

（a） Mode 1

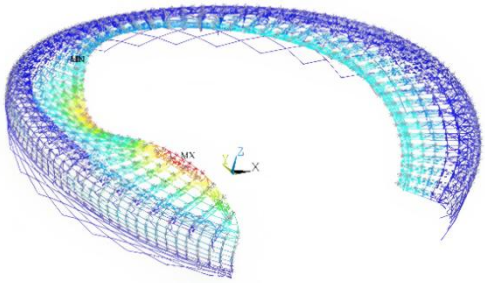

（b） Mode 2

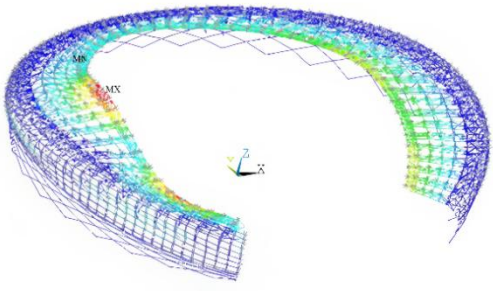

（c） Mode 3

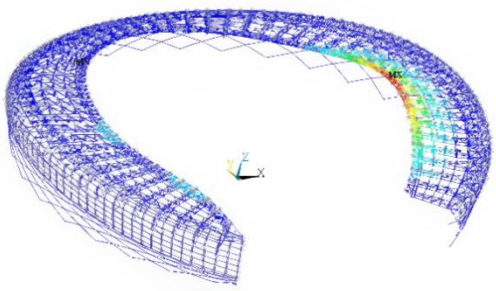

（d） Mode 4

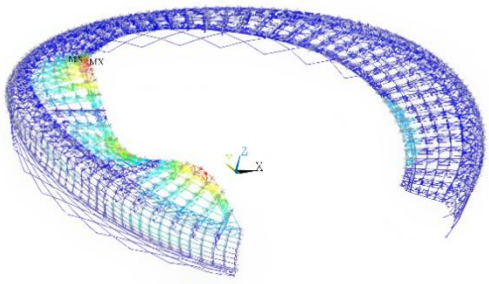

（e） Mode 5

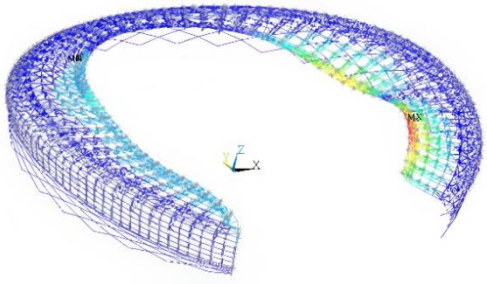

（f） Mode 6

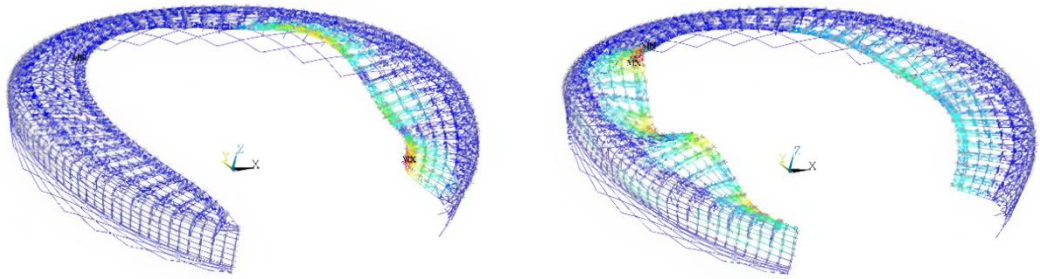

（g） Mode 7　　（h） Mode 8

Fig. 4 Separated steel canopy first 8 modes vibration mode diagram

From the modal information listed in Table 1: 1) the vibration modes with higher mass participation factors are the 4th and 1st modes. As seen in Fig. 4, these two modes mainly exhibit vertical deformation in major areas of the east and west cantilevers. 2) The 7th and 5th stage modes correspond to the third and fourth highest mass participation factors, respectively. They demonstrate vertical deformation at minor openings within eastern and western cantilevers, causing waveform distortions in adjacent regions.3) The remaining vibration modes are primarily characterized by vertical waveform deformation in other eastern and western zones.

(2) Modal analysis of integrated model

The self-vibration frequencies, periods, and mass participation factors for the top 20 modes of the integrated model are shown in Table 2 below.

From Table 2 it can be seen that the first 8 modes of the main vibration mode of the integrated structure, with a mass fraction of 80%, is smaller than the proportion of the first 8 modes of the vibration mode of the independent steel structure. The self-vibration mode of the first 8 modes of the structure is shown in Fig. 5.

Table 2
Modal analysis information of the integrated model

Number of modes	Frequency（Hz）	Periods（s）	Mass participation factor（%）
1	1.10	0.91	9.02
2	1.11	0.90	8.89
3	1.21	0.83	0.57
4	1.23	0.81	0.02
5	1.29	0.77	0.01
6	1.38	0.72	0.06
7	1.42	0.70	3.33
8	1.45	0.69	0.40
9	1.53	0.65	1.50
10	1.54	0.65	0.47
11	1.55	0.64	0.09
12	1.71	0.59	0.01
13	1.79	0.56	0.03
14	1.89	0.53	0.12
15	1.94	0.52	0.01
16	2.10	0.48	0.10
17	2.12	0.47	0.04
18	2.17	0.46	2.62
19	2.21	0.45	0.45
20	2.29	0.44	0.07

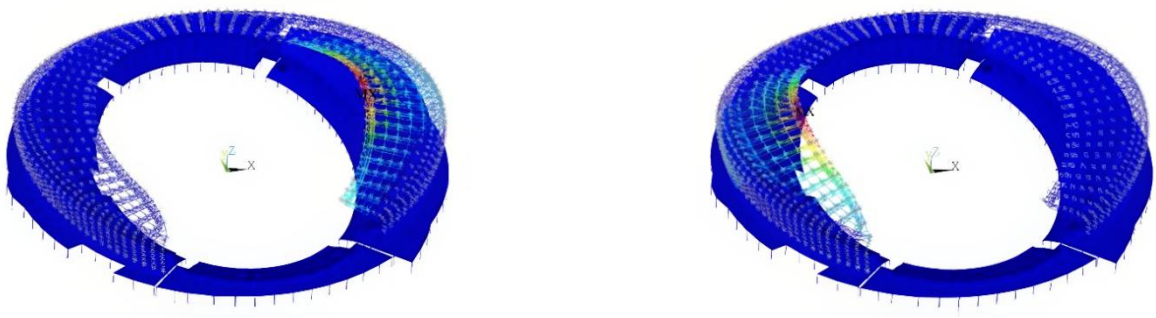

(a) Mode 1　　(b) Mode 2

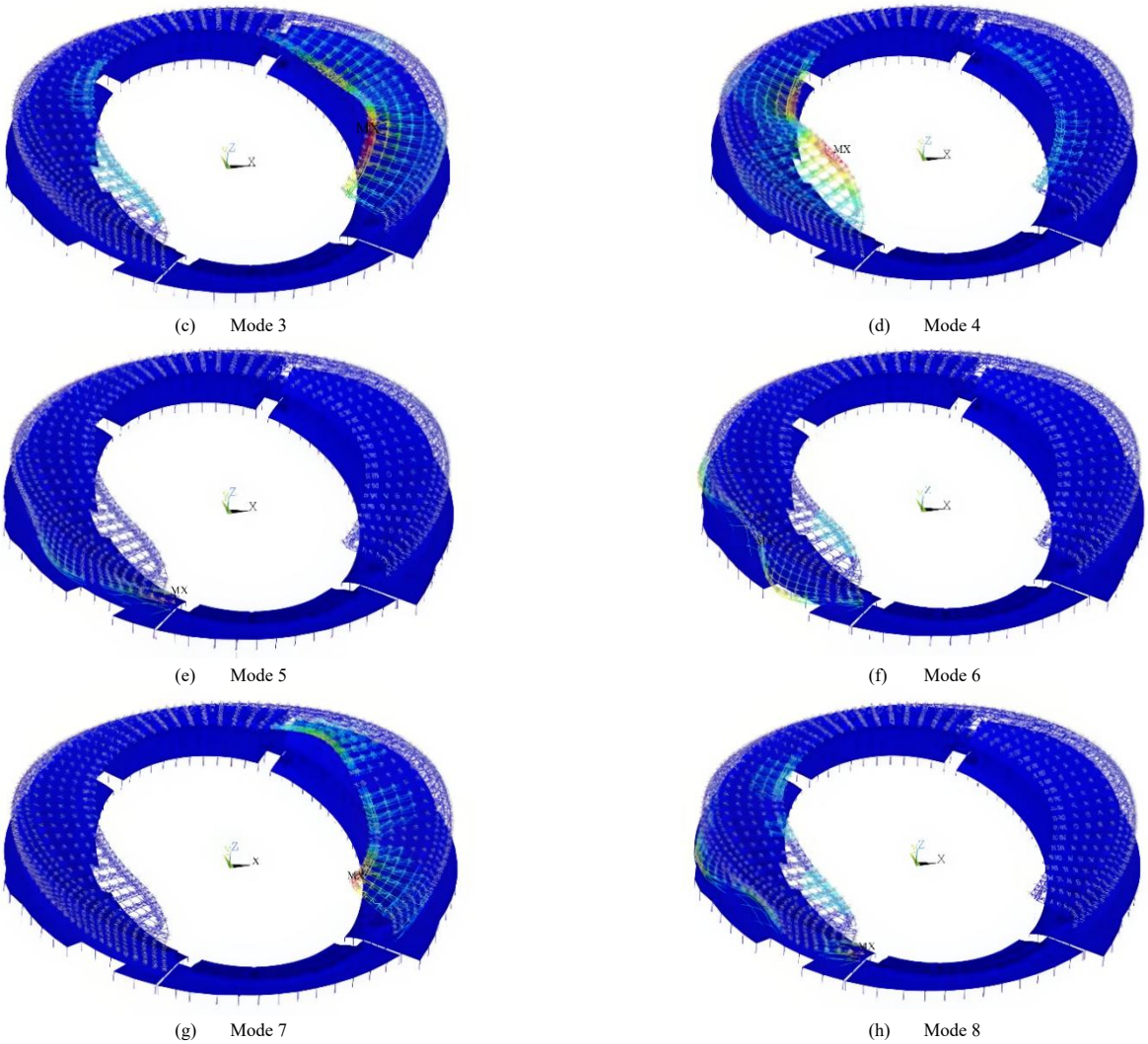

(c) Mode 3 (d) Mode 4

(e) Mode 5 (f) Mode 6

(g) Mode 7 (h) Mode 8

Fig. 5 The first 8 modes vibration mode diagram of the integrated model

From the modal information listed in Table 2, it can be seen that 1) the vibration mode with the highest mass participation factor is the 1st mode, followed by the 2nd mode. As seen in Fig. 5, this two-mode predominantly exhibit vertical deformation in major cantilevered areas of the eastern and western spans. 2) The 7th mode corresponds to the third-highest mass participation factor, displaying vertical deformation at minor openings within eastern cantilevers and inducing waveform distortions in the surrounding areas. 3) The 3rd and 4th mode shows continuous fluctuating vertical deformation in other cantilever areas.

The main vibration modes of the integrated structure and the separated steel canopy are concentrated in the first 8th modes, accounting for 80% and 85% mass participation respectively. While both systems exhibit vertical deformation in major east-west pipe trusses for their first two stage modes, the integrated model's longer self-vibration period period (0.91s vs. 0.75s) indicates that it has less stiffness. Moreover, localized deformation of the facade structure occurs in the vibration mode of the integrated structure. The modal analysis results of these two models are different to some extent.

The physical essence of the natural frequency differences between the integrated and separated models stems from a threefold stiffness enhancement mechanism induced by coupling effects:

1) Stiffness Reconfiguration. The separated model assumes hinged connections (transmitting only vertical forces) between the canopy and stands, neglecting the flexural capacity of nodes. In the integrated model, bidirectional constraints at welded nodes strengthen the off-diagonal terms of the stiffness matrix, directly enhancing the integrated stiffness.

2) Modal Fusion. The independent vibrations in the separated model (vertical bending of the canopy and horizontal sway of the stands) couple into a synergistic lateral displacement mode in the integrated model. The stiffer force-transfer path of this new modal configuration elevates the fundamental frequency.

3) Mass-Stiffness Equilibrium. While the added mass of interface components tends to decrease frequencies, the stiffness reinforcement effect consistently dominates, leading to a higher fundamental frequency in the integrated model. This phenomenon can be analogized to the coupled vibration of a string and a resonance box. The separated model only excites local vibrations of the canopy, whereas the integrated model establishes a complete energy transfer chain, thereby amplifying the fundamental frequency response.

2.3. Ground motion selection

The seismic fortification intensity of this project is 7 degrees, and the fundamental seismic acceleration value is 0.10g. The site is classified as Seismic Group 2, Site Class II, featuring a characteristic period of 0.40s.

Based on the seismic design parameters and structural self-vibration characteristics, seven ground motions were selected for analysis (Table 3). The standard response spectrum curve, the ground motion response spectrum curve, and its average spectrum curve are illustrated in Figure 6. The average spectrum maintains less than 30% deviation from the standard spectrum, satisfying, ASCE7-10[47] Requirements. The seven ground motions listed in Table 3 were rigorously selected to match the seismic site characteristics of the large stadium [43].

1.Soil Type: All records have V_{S30} values (213 - 356 m/s), which encompass the range for Class II medium-stiff soil (V_{S30} = 180 - 375 m/s).

2.Magnitude Range: The moment magnitudes (M_w 6.7 - 7.6) correspond to the site's design basis earthquake (M_w 7.0 ± 0.3) and rare earthquake (M_w 7.5) levels.

3.Risk Coverage: The selection includes scenarios such as near-fault pulse (Northridge), basin effect (Kobe), and deep-source seismicity (Victoria, Mexico). These systematically examine the canopy's structural vulnerabilities across diverse hazard conditions. The names of the later ground motions are simplified to EL, NR, KB, TF, WL, CC and VM.

Table 3
Ground motion records

No.	Name	Date	Station	Magnitude
1	EL Centro	1940	EL Centro Array #9	7.0
2	Northridge	1994	Arleta - Nordhoff Fire Sta	6.6
3	Kobe	1995	Takarazuka	6.9
4	Taft	1952	Taft Lincoln School	7.4
5	Wo Long	2008	051WCW 31.04N 103.18E	8.0
6	CHICHI	1999	TCU122	7.6
7	Victoria Mexico	1980	Cerro Pricto	6.4

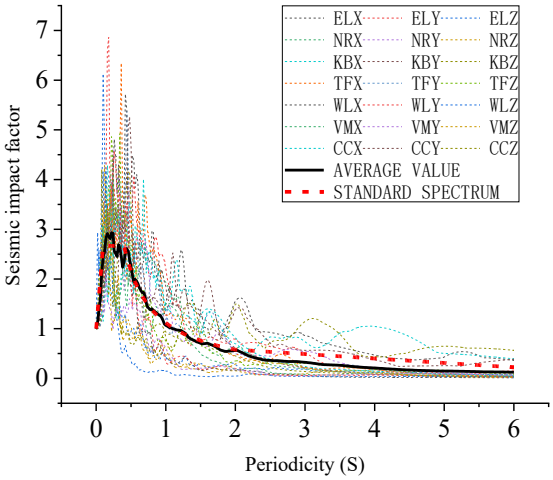

Fig. 6 Spectral curves of seismic effect coefficients for different ground motion

To study the seismic performance of the steel canopy structure and investigate the effects of different types of ground motion and peak acceleration on the structure, time history analysis is employed in this paper. The stress time histories of the critical members and the displacement time histories of the necessary nodes are calculated. The peak ground motion acceleration is adjusted in the X, Y, and Z directions in a 1:0.85:0.65 ratio [43]. Time history analysis was performed using peak acceleration at 50 gal, 100 gal, 200 gal and 300 gal.

3. Steel canopy computational model time-range analysis results comparison

3.1. Maximum value of the dynamic response and comparison methods

To ensure analytical accuracy, Fig. 7 identifies the monitored pipe trusses and measurement point locations. Because the most severe dynamic response of model A is under Taft ground motion, this is used as an example to illustrate the comparative analysis method of the dynamic response for the three models. The structural dynamic response of Model A under 100 gal Taft ground motion is shown in Figs. 8(a) and (b).

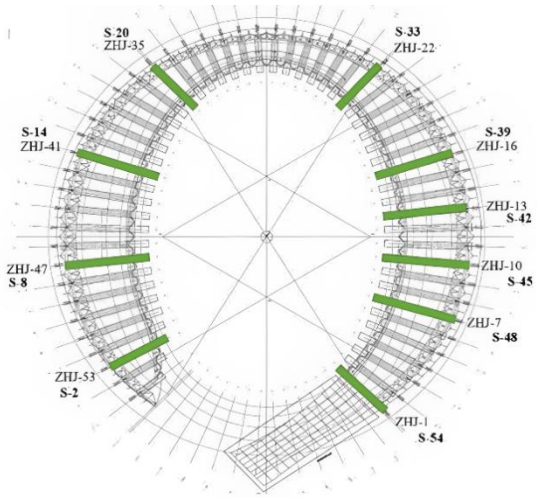

(a) Plan position of pipe trusses

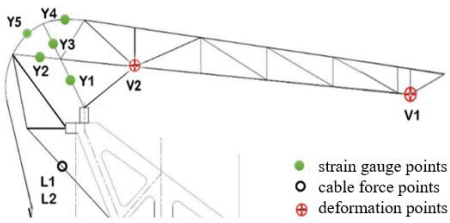

(b) Location of measuring points

Fig. 7 Pipe truss monitoring location

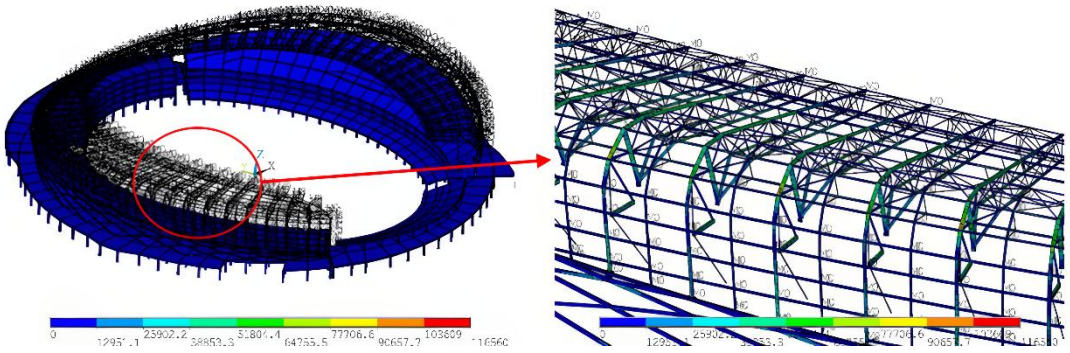

(a)stress chart

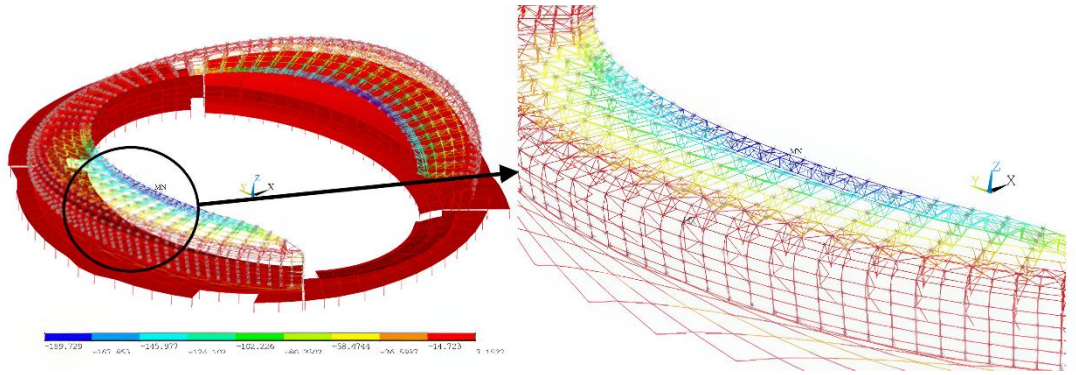

(b) transformation chart

Fig. 8 Structural dynamic response under Taft ground motion for model A 100 gal

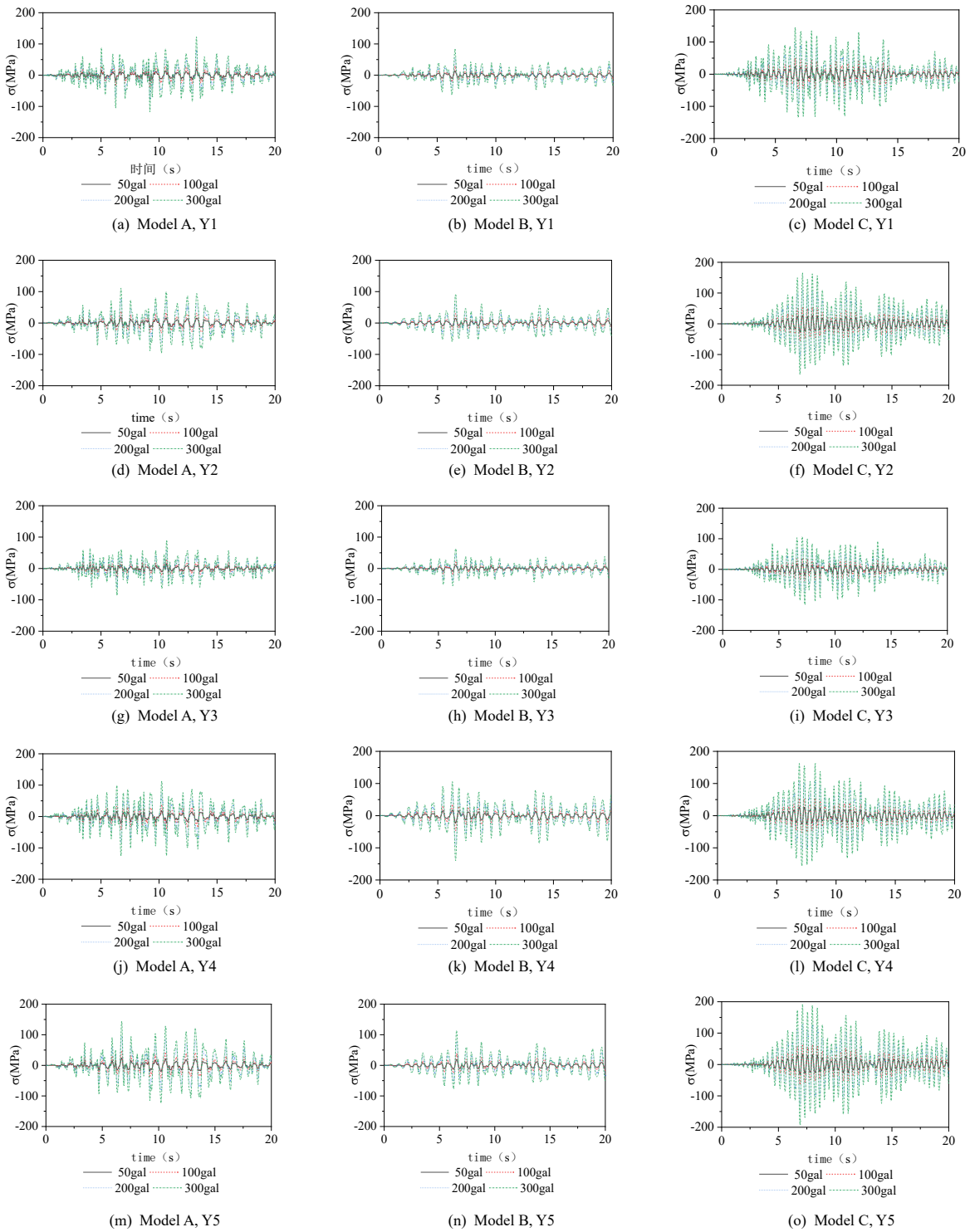

Fig. 9 Stress time history curves of crucial components of ZHJ-47 in three model analyses

Table 4
Maximum stresses and comparison of critical members of ZHJ-47 truss under Taft ground motion with three analytical models (MPa)

Critical members	Peak acceleration（gal）	σA（MPa）	σB（MPa）	σC（MPa）	σB/σA	σC/σA
Y1	50	20.41	14.09	24.33	0.69	1.19
	100	40.81	28.18	48.66	0.69	1.19
	200	81.62	56.36	97.33	0.69	1.19
	300	122.43	84.55	145.99	0.69	1.19
Y2	50	18.56	15.05	27.68	0.81	1.49
	100	37.11	30.11	55.36	0.81	1.49
	200	74.23	60.21	110.73	0.81	1.49
	300	111.34	90.32	166.09	0.81	1.49
Y3	50	14.82	10.51	17.75	0.71	1.20
	100	29.65	21.02	35.50	0.71	1.20
	200	59.29	42.04	70.99	0.71	1.20
	300	88.94	63.06	106.49	0.71	1.20
Y4	50	18.90	17.59	27.07	0.93	1.43
	100	37.81	35.19	54.13	0.93	1.43
	200	75.61	70.38	108.26	0.93	1.43
	300	113.42	105.57	162.35	0.93	1.43
Y5	50	24.06	18.98	32.11	0.79	1.33
	100	48.13	37.96	64.18	0.79	1.33
	200	96.25	75.92	128.36	0.79	1.33
	300	144.38	113.88	192.54	0.79	1.33

Fig. 8 identifies the maximum stress of 116.56 MPa at the critical member near the support, while the maximum deformation of 189.72 mm occurs at the longest cantilevered truss. Taft ground motions with peak accelerations of 50-gal, 100-gal, 200-gal, and 300-gal were input to Models A, B, and C. The maximum stresses and vertical displacements of this pipe truss are used as an example to illustrate the differences between Models B, C, and Model A.

（1）Comparative analysis of peak stresses in critical members of ZHJ-47 pipe truss under Taft ground motion.

The positions of critical members Y1, Y2, Y3, Y4, and Y5 of the ZHJ-47 pipe truss were obtained under Taft ground motion stimulation, as shown in Fig. 7(b). The stress time history curves are shown in Fig. 9. The stress limits for each member were extracted and included in Table 4.

As can be seen from Table 4: 1) For peak ground accelerations ⩽300 gal, peak stresses in all three models exhibit linear growth with increasing acceleration.; 2) The maximum value of C model stress is 192.54 MPa under 300-gal ground motion, equivalent to 65.3% of the design value of steel strength; 3) The stresses in Model B are 0.79 times higher on average than those in Model A. The stresses in Model C are 1.33 times higher on average than Model A. As a result, Model B's calculations are biased toward insecurity, and Model C's calculations are biased toward conservatism compared to the integrated model A.

(2) The displacement time history curve of the cantilevered end of ZHJ-47 pipe truss is obtained under the excitation of Taft ground motion, shown in Fig. 10. Extracted vertical displacement extremes for endpoint V1 are listed in Table 5.

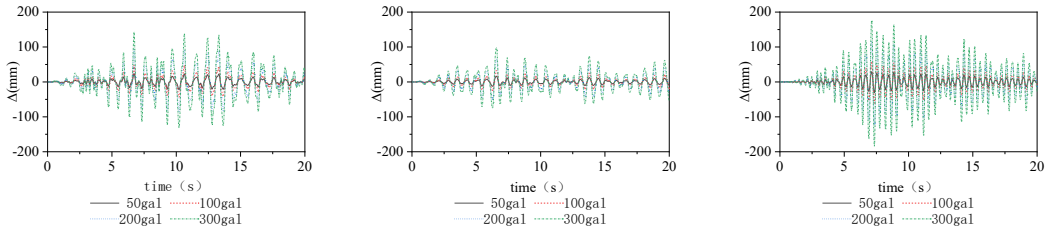

(a) Model A (b) Model B (c) Model C

Fig. 10 Displacement time history curves of ZHJ-47 cantilever point V1 in three model analyses

Table 5
Maximum deflection at the cantilever point and comparison of three models of ZHJ-47 under Taft ground motion（mm）

Peak acceleration（gal）	Δ_A（mm）	Δ_B（mm）	Δ_C（mm）	Δ_B/Δ_A	Δ_C/Δ_A
50	23.89	16.38	29.29	0.69	1.23
100	47.78	32.76	58.58	0.69	1.23
200	95.56	65.52	117.16	0.69	1.23
300	143.34	98.28	175.74	0.69	1.23

Table 5 demonstrates: 1) T Maximum displacements at the cantilever end increase linearly with peak acceleration for all three models, confirming their elastic response range.2) According to the linear interpolation, the maximum deflections are 33.45mm and 105.12mm, respectively, for 8-degree multiple earthquakes of 70 gal and a 7-degree rare earthquake of 220 gal. The results were 1/1184 and 1/377 of the cantilever length, which meets norm requirements.[43] The average deflection of Model B is 0.69 times higher than that of Model A, while Model C averages 1.23 times higher. The results indicate that the calculation results of model B are unreliable, and those of model C are conservative.

Based on the dynamic responses calculated from the three models under Taft ground motion, the steel canopy structure has better seismic performance. To further analyze the differences in seismic performance among the three models, the two trusses with larger spans, ZHJ-10 and ZHJ-47, and the truss with smaller spans, ZHJ-22, were selected. The time history curves under seven kinds of ground motion excitation are obtained. Using the results of model A calculations as a benchmark, the change rule for maximum stresses of critical members Y1 - Y5, and the maximum deflection of the cantilever point V1 in the three models are analyzed to investigate a simplified calculation method for the seismic performance of steel canopy structures.

3.2. Stress comparison analysis of critical members

Based on the calculation results of the three analytical models, the peak stresses of the critical members for the three tube trusses ZHJ-10, 22, and 47 are extracted. The maximum stresses of Model B and Model C were compared with Model A, which is shown in Fig. 11. Analysis reveals:

1) As the peak acceleration increases, most Model B to Model A maximum stress ratios are less than 1.0, indicating that the stresses in the critical members obtained from the analysis of Model B are less than that of Model A. The calculation results are not safe.

2) As the peak acceleration increases, most Model B to Model A maximum stress ratios are more than 1.0, indicating that the stresses in the vital members obtained from the analysis of Model C are more than that of Model A. The calculation results are conservative.

3) The stresses derived from simplified Models B and C respectively provide lower-bound and upper-bound estimates of Model A results, establishing validated reference values for structural preliminary design.

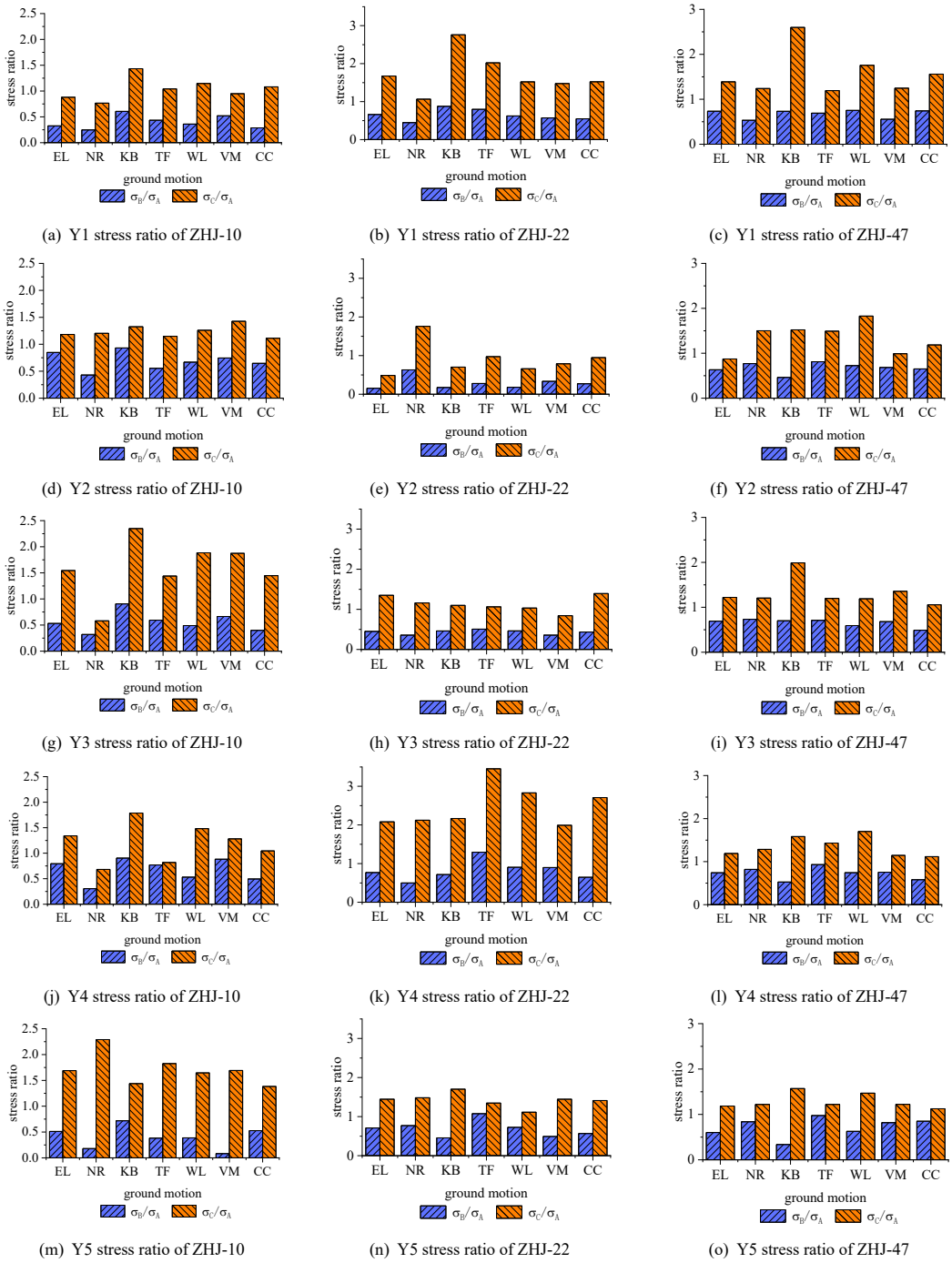

(a) Y1 stress ratio of ZHJ-10 (b) Y1 stress ratio of ZHJ-22 (c) Y1 stress ratio of ZHJ-47

(d) Y2 stress ratio of ZHJ-10 (e) Y2 stress ratio of ZHJ-22 (f) Y2 stress ratio of ZHJ-47

(g) Y3 stress ratio of ZHJ-10 (h) Y3 stress ratio of ZHJ-22 (i) Y3 stress ratio of ZHJ-47

(j) Y4 stress ratio of ZHJ-10 (k) Y4 stress ratio of ZHJ-22 (l) Y4 stress ratio of ZHJ-47

(m) Y5 stress ratio of ZHJ-10 (n) Y5 stress ratio of ZHJ-22 (o) Y5 stress ratio of ZHJ-47

Fig. 11 Maximum stress ratios of critical members in the three analytical models

3.3. Comparative analysis of deflection at the cantilever point

Based on the calculation results of the three analytical models, the peak vertical displacements at the cantilever ends are extracted. The maximum displacements of models B and C are compared with model A. Trend plots of the maximum displacement ratios of model B and C versus model A for the three pipe trusses under seven ground motions are shown in Fig. 12.

It can be seen from Fig. 12 that, as the peak acceleration increases:

1) Most of the maximum displacement ratios of the three tube truss cantilever points in Model B and Model A showed a trend of less than 1.0, indicating that the displacement of the cantilever point obtained from the analysis of Model B is smaller than that of Model A.

2) Most of the maximum displacement ratios of the three pipe truss cantilevering points in Model C and Model A showed a trend of more than 1.0 for most of the models, indicating that the displacement of the cantilever point obtained from the analysis of Model C is larger than that of Model A.

In summary, all three models' dynamic responses satisfy design requirements, validating satisfactory seismic resilience of the steel canopy structure.

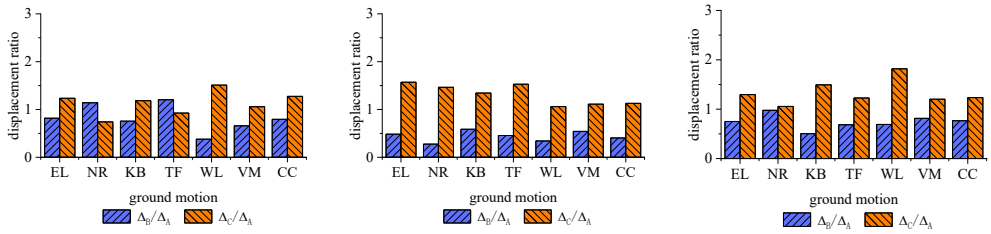

(a) ZHJ-10 (b) ZHJ-22 (c) ZHJ-47

Fig. 12 Maximum vertical displacement ratio of three types of pipe trusses

4. Simplified calculations of the dynamic response of steel canopy structure in elastic stage

Seven ground motions were selected for time history analysis of three computational models at four peak acceleration values (50-gal, 100-gal, 200 gal and 300 gal). Peak stresses at critical members and maximum displacements at cantilever ends were extracted for three typical tube trusses. With the increase in peak ground motion, both stress and displacement exhibit a linear growth trend, indicating that the structure is currently operating within its elastic range. Based on this, a simplified computational method is proposed to investigate the relationship between the computational model and two simplified models. Furthermore, the results of the simplified model calculations can reduce computational costs, which provides a reference for the preliminary design of the integrated structure.

4.1. Simplified calculation method for integrated model stresses

Under the influence of seven ground motions, with an acceleration peak of 100 gal, three computational models are selected to analyze the maximum stress in critical members. They are listed the in Tables. 6, 7, and 8, respectively.

Table 6
Model A critical member stress (MPa)

Truss number	Member number	ground motion						
		EL	NR	KB	TF	WL	VM	CC
ZHJ-10	Y1	34.57	22.72	29.72	42.27	28.41	18.17	30.49
	Y2	53.13	34.03	50.67	52.98	34.65	22.02	34.88
	Y3	17.40	13.24	18.79	27.49	16.02	9.16	20.48
	Y4	23.95	23.72	24.87	39.81	18.56	14.48	30.34
	Y5	20.60	14.78	23.49	37.73	10.43	24.49	26.41
ZHJ-22	Y1	12.47	9.47	11.24	10.63	14.94	8.09	15.48
	Y2	15.02	12.71	15.48	17.71	18.48	7.62	11.94
	Y3	11.63	8.62	14.71	13.40	13.94	7.32	11.17
	Y4	17.02	8.16	21.25	12.55	12.24	8.24	16.09
	Y5	18.71	14.75	26.83	29.38	31.92	27.03	29.07
ZHJ-47	Y1	35.34	30.18	30.26	40.81	25.87	22.18	28.34
	Y2	47.20	30.42	40.66	37.11	25.41	20.94	35.73
	Y3	25.18	19.87	27.26	29.65	28.88	12.55	31.49
	Y4	41.35	29.49	41.35	37.81	28.88	20.71	42.89
	Y5	43.74	31.45	44.08	48.32	42.08	37.69	62.14

Table 7
Model B critical member stress (MPa)

Truss number	Member number	ground motion						
		EL	NR	KB	TF	WL	VM	CC
ZHJ-10	Y1	11.24	5.62	18.02	18.40	10.24	9.47	8.78
	Y2	45.05	14.63	47.20	29.34	23.18	16.40	22.56
	Y3	9.24	4.24	17.02	16.32	7.85	6.08	8.16
	Y4	19.02	7.24	22.48	30.65	9.86	12.78	15.02
	Y5	10.55	2.66	16.86	14.40	4.04	2.00	13.94
ZHJ-22	Y1	8.24	4.24	9.86	8.47	9.32	4.62	8.47
	Y2	2.31	8.01	2.70	4.93	3.31	2.54	3.23
	Y3	5.24	3.08	6.78	6.78	6.47	2.62	4.85
	Y4	13.09	4.08	15.25	16.25	11.09	7.39	10.40
	Y5	13.28	11.36	12.24	31.61	23.18	13.28	16.48
ZHJ-47	Y1	25.95	16.09	22.18	28.18	19.48	12.32	21.02
	Y2	29.88	23.41	18.79	30.11	18.40	14.32	23.25
	Y3	17.40	14.55	19.10	21.02	17.09	8.55	15.40
	Y4	30.65	24.18	21.79	35.19	21.48	15.63	24.87
	Y5	26.33	26.41	14.86	47.12	26.41	30.88	52.86

Table 8
Model C critical member stress (MPa)

Truss number	Member number	ground motion						
		EL	NR	KB	TF	WL	VM	CC
ZHJ-10	Y1	30.42	17.40	42.58	44.04	32.57	17.25	32.96
	Y2	62.87	40.96	67.14	60.79	43.66	31.42	38.85
	Y3	26.87	7.70	44.12	39.58	30.18	17.17	29.65
	Y4	32.11	16.17	44.43	32.57	27.49	18.56	31.72
	Y5	34.80	33.84	33.76	68.88	17.17	41.43	36.54
ZHJ-22	Y1	20.87	10.09	31.03	21.48	22.72	11.94	23.56
	Y2	7.32	22.33	10.86	17.25	12.17	6.01	11.32
	Y3	15.71	10.01	16.17	14.25	14.40	6.16	15.55
	Y4	35.42	17.33	46.05	43.35	34.65	16.40	43.58
	Y5	27.07	21.87	45.66	39.54	35.54	39.08	41.00
ZHJ-47	Y1	49.05	37.42	78.62	48.66	45.43	27.64	44.20
	Y2	41.20	45.66	61.83	55.36	46.43	20.71	42.35
	Y3	30.72	23.91	54.21	35.50	34.34	17.02	33.26
	Y4	49.20	37.88	65.45	54.13	49.13	23.72	47.89
	Y5	51.82	38.38	69.22	58.98	61.79	46.05	69.95

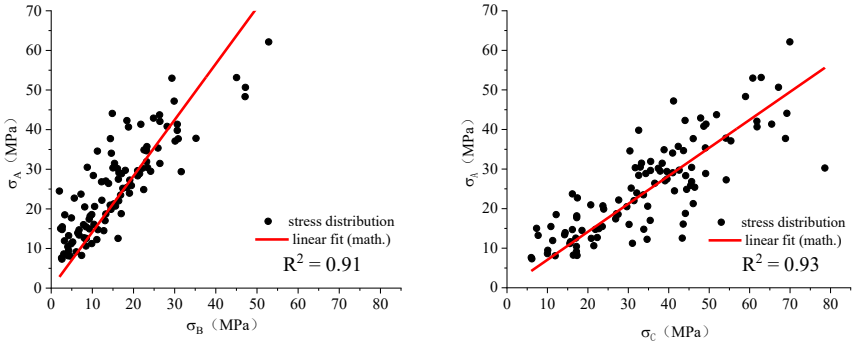

(a) Model B & Model A (b) Model C & Model A

Fig. 13 Stress distribution and linear fitting of models B and C to model A

The stress distributions of the critical components of models B and A, as well as models C and A are shown in the form of scatter plots as shown in Fig. 13. And the proportionality equations of σ_A vs. σ_B and σ_A vs. σ_C are fitted.

As shown in Fig. 13(a), the stress distributions of models B and A are linearly distributed. The slope of the fitted line is 1.42 > 1, which indicates that Model B underestimates stresses versus Model A. R^2 = 0.91 indicates that the fitting accuracy is a bit reasonable.

As shown in Fig. 13(b), the stress distributions of model C and model A are also linearly distributed. The slope of the fitted line is 0.71 < 1, indicating that Model C overestimates stresses versus Model A. R^2 = 0.93 indicates a reasonable fitting accuracy. Therefore, the stress relationship between models B/C and model A can be approximated by the following calculation equation:

$$\sigma_A = 1.42 \times \sigma_B \quad (4)$$

$$\sigma_A = 0.71 \times \sigma_C \quad (5)$$

In the equation, σ_A、 σ_B and σ_C which are obtained from time history analysis under a specific peak acceleration represent the maximum stress values of the members in models A, B, and C, respectively..

Stress ratios σ_A/σ_B and σ_A/σ_C for the critical members of the three pipe trusses in Model A, B, and C are listed in Table 9 and 10, respectively.

As can be seen in Table 9, the σ_A/σ_B data are in the vicinity of the factor 1.42 in the computational equation (4), except for individual data with large deviations. This distribution indicates validity of the fitted equation.

Table 9
Stress ratios in critical members of Model A and Model B

Truss number	Member number	ground motion						
		EL	NR	KB	TF	WL	VM	CC
ZHJ-10	Y1	3.03	4.00	1.64	2.27	2.78	1.92	3.45
	Y2	1.18	2.33	1.08	1.82	1.49	1.35	1.54
	Y3	1.89	3.13	1.10	1.69	2.04	1.52	2.50
	Y4	1.27	3.23	1.11	1.30	1.89	1.14	2.00
	Y5	1.96	5.56	1.39	2.63	2.56	12.50	1.89
ZHJ-22	Y1	1.52	2.22	1.14	1.25	1.61	1.75	1.82
	Y2	6.67	1.59	5.88	3.57	5.56	3.03	3.70
	Y3	2.22	2.78	2.17	1.96	2.17	2.78	2.33
	Y4	1.30	2.00	1.39	0.78	1.10	1.11	1.54

	Y5	1.41	1.30	2.17	0.93	1.37	2.04	1.75
ZHJ-47	Y1	1.37	1.89	1.37	1.45	1.33	1.79	1.35
	Y2	1.59	1.30	2.17	1.23	1.39	1.47	1.54
	Y3	1.45	1.37	1.43	1.41	1.69	1.47	2.04
	Y4	1.35	1.22	1.89	1.08	1.35	1.33	1.72
	Y5	1.67	1.19	2.94	1.02	1.59	1.22	1.18

Table 10
Stress ratios in critical members of model A and model C

Truss number	Member number	ground motion						
		EL	NR	KB	TF	WL	VM	CC
ZHJ-10	Y1	1.14	1.30	0.70	0.96	0.87	1.05	0.93
	Y2	0.85	0.83	0.75	0.87	0.79	0.70	0.90
	Y3	0.65	1.72	0.43	0.69	0.53	0.53	0.69
	Y4	0.75	1.47	0.56	1.22	0.68	0.78	0.95
	Y5	0.59	0.44	0.69	0.55	0.61	0.59	0.72
ZHJ-22	Y1	0.60	0.93	0.36	0.50	0.66	0.68	0.66
	Y2	2.04	0.57	1.43	1.03	1.52	1.27	1.05
	Y3	0.74	0.86	0.91	0.94	0.97	1.19	0.72
	Y4	0.48	0.47	0.46	0.29	0.35	0.50	0.37
	Y5	0.69	0.68	0.59	0.74	0.90	0.69	0.71
ZHJ-47	Y1	0.72	0.81	0.38	0.84	0.57	0.80	0.64
	Y2	1.15	0.67	0.66	0.67	0.55	1.01	0.84
	Y3	0.82	0.83	0.50	0.83	0.84	0.74	0.94
	Y4	0.84	0.78	0.63	0.70	0.59	0.87	0.89
	Y5	0.85	0.82	0.64	0.82	0.68	0.82	0.88

As can be seen from Table 10, except for individual data with large deviations, the σ_A/σ_C data are in the vicinity of the coefficient 0.71 in the calculated equation (5), indicating that the fitted calculated equation is more reasonable. It also indicates validity of the fitted equation.

4.2. Simplified calculation method for integrated model displacement

It is similar to the simplified calculation method for the stresses of the integrated model. Under the influence of seven ground motions, with an acceleration peak of 100 gal, three computational models are selected to analyze the maximum displacement of the cantilever end. They are listed in Table 11, Table. 12, and Table. 13, respectively.

Table 11
Model A critical member displacement (mm)

Truss number	ground motion						
	EL	NR	KB	TF	WL	VM	CC
ZHJ-10	22.63	6.71	26.02	23.40	15.71	13.92	14.12
ZHJ-22	7.07	2.98	9.55	13.12	12.94	5.42	11.06
ZHJ-47	35.66	24.05	33.28	47.78	31.72	19.11	33.60

Table 12
Model B critical member displacement (mm)

Truss number	ground motion						
	EL	NR	KB	TF	WL	VM	CC
ZHJ-10	18.50	7.64	19.68	28.18	5.94	9.18	11.22
ZHJ-22	3.42	0.82	5.60	5.98	4.42	2.94	4.48
ZHJ-47	26.76	23.50	16.82	32.76	21.94	15.58	25.74

Table 13
Model C critical member displacement (mm)

Truss number	ground motion						
	EL	NR	KB	TF	WL	VM	CC
ZHJ-10	27.92	4.96	30.78	21.64	23.7	14.72	18
ZHJ-22	11.12	4.36	12.82	20.06	13.72	6.02	12.48
ZHJ-47	46.24	25.38	49.7	58.58	57.68	22.98	41.48

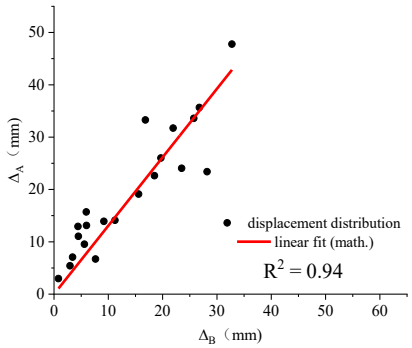

(a) Model B and Model A displacement distributions and linear fitting

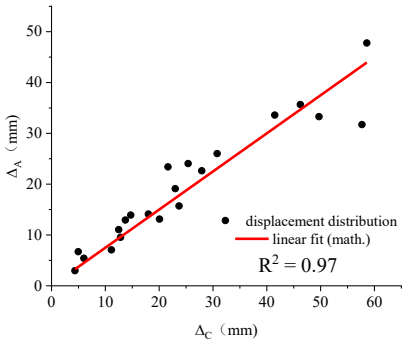

(b) Model C and Model A displacement distributions and linear fitting

Fig. 14 Model B and Model C with Model A displacement distribution and linear fit law, respectively

The displacement distribution of models B and A, as well as models C and A are shown in the form of scatter plots, respectively. It is shown in Fig. 14. And the proportionality equations of σ_A vs. σ_B and σ_A vs. σ_C are fitted.

As can be seen from Fig. 14(a), the displacement distributions of model B and model A are linearly distributed. The slope of the fitted line is 1.31 > 1, which indicates that Model B's displacement is less than Model A. $R^2 = 0.94$ indicates that the fitting accuracy is reasonable.

As can be seen from Fig. 14(b), the displacement distributions of model C and model A are linearly distributed. The slope of the fitted line is 0.75 < 1, which indicates that Model C's displacement is more than Model A. $R^2 = 0.97$ indicates that the fitting accuracy is reasonable. Therefore, the relationship between model B, C and model A can be expressed as follows:

$$\Delta_A = 1.31 \times \Delta_B \quad (6)$$

$$\Delta_A = 0.75 \times \Delta_C \quad (7)$$

In the equation, Δ_A, Δ_B and Δ_C are the maximum displacements at the cantilever end of the pipe truss obtained from time history analysis at a certain peak acceleration.

The displacement ratios of the cantilever end between Model A and Model B, as well as between Model A and Model C, are listed in Table 14 and 15, respectively.

Table 14
Displacement ratio between Model A and Model B cantilevered ends

Truss number	ground motion						
	EL	NR	KB	TF	WL	VM	CC
ZHJ-10	1.22	0.88	1.32	0.83	2.63	1.52	1.27
ZHJ-22	2.08	3.57	1.69	2.17	2.94	1.85	2.44
ZHJ-47	1.33	1.02	1.96	1.45	1.45	1.22	1.30

Table 15
Displacement ratio between Model A and Model C cantilevered ends

Truss number	ground motion						
	EL	NR	KB	TF	WL	VM	CC
ZHJ-10	0.81	1.35	0.85	1.09	0.66	0.94	0.79
ZHJ-22	0.64	0.68	0.75	0.65	0.94	0.90	0.88
ZHJ-47	0.77	0.94	0.67	0.81	0.55	0.83	0.81

As can be seen from Table 14 and 15, the displacement ratios in the Table are close to 1.31 and 0.75 in the displacement calculation equations (6) and (7), except for deviations in individual data. It indicates that the computational equation is fitted well.

To further validate the reliability and applicability of Equations (4)-(7), a comparative verification was conducted using published shaking table test data [48]. The case study adopted a modeling approach analogous to this paper, employing both integrated and separated models for computational analysis. Finite element analyses are performed on Lushan Middle School Gymnasium and Lushan County Gymnasium, utilizing ground motion records from actual seismic stations in earthquake-affected regions. By substituting the stresses and key displacements acquired from the three models (the integrated model and the two separated models) of each gymnasium into the equations, a good agreement was observed between the test data and the formula predictions, confirming that the simplified equations accurately reflect the fundamental behavioral relationships between the integrated and separated models of steel canopies in large stadium structures.

5. Analysis of the lower support structure influencing dynamic response

The comparative analysis of dynamic responses between simplified and integrated steel canopy structure models demonstrates that Model B (considering the lower support structure as rigid) and Model C (inputting average ground motion responses of lower support columns to the upper steel canopy structure) are both different from the calculation results of the integrated model. Therefore, it is necessary to analyze the fundamental mechanisms of the lower support structure's influence on the dynamic response of the steel canopy structure.

This section calculates the three-directional stiffness of the lower support structure at the steel canopy supports and quantifies the peak and frequency changes induced by ground motion passing through the structure. It further examines the effects of lower support structure stiffness in-homogeneity, amplification effect, and filtering effect of ground motion acceleration on the dynamic responses of all three models. The results show that there are differences between the three models.

5.1. Support stiffness in-homogeneity effect

Differences in constructing various frames of the lower support structure cause in-homogeneous stiffness at different steel canopy structure supports. This resulted in an inconsistent dynamic response output to the steel canopy structure at each support under ground motion excitation. Furthermore, it has an impact on the dynamic response of the steel canopy structure, and this phenomenon is referred to as the support stiffness in-homogeneity effect.

A primary cause of support stiffness in-homogeneity stems from construction tolerances during the actual fabrication and installation of support nodes, as well as material and manufacturing variability in support components (e.g., elastic pads, pins, connecting plates).

1) Quantitative Impact of Construction Tolerances

Inevitably, construction deviations occur in the support positioning (planar

location and elevation) and assembly clearances of key components (e.g., clearances between pins and sleeves and gasket thickness between connecting plates). According to the Code for Construction Quality Acceptance of Steel Structure Engineering [49] and related standards [50-51], dimensional tolerances for key nodes in large steel structures typically range from ±3 mm to ±5 mm for installation positions and ±0.5 mm to ±1.0 mm for assembly clearances. Such minor geometric deviations significantly alter the actual constraint conditions of supports (e.g., boundary clearance changes directly affect sliding resistance and rotational restraint) and the effective load-transfer path length (influencing the effective length L_e in axial and bending stiffness formulas), causing the in-service effective horizontal and rotational stiffness to deviate from design values.

2) Quantitative Impact of Material/Manufacturing Variability

Key properties of supports (e.g., the shear modulus G of rubber pads, the elastic modulus E of metal parts, and the friction coefficient μ of sliding materials) exhibit inherent property dispersion due to manufacturing tolerances. For rubber supports: their designed shear modulus G typically allows for manufacturing deviations of ±15% or higher [52]. Since the shear stiffness $K \approx G \cdot A/t$ (where A is the rubber bearing area and t is the net of rubber layers height), such G-value deviations directly lead to stiffness fluctuations exceeding ± 15%. Similarly, minor volatility (e.g., ±1% - 2%) in the dimensional accuracy (e.g., thickness, hole diameter) of metal components during manufacturing will affect their contribution to composite stiffness by altering cross-sectional properties.

Therefore, the main difference between the integrated model A, which considers the coupling effect of the lower support structure, and the simplified analytical models B/C lies in their boundary assumptions: Model B presumes infinitely rigid supports (zero displacement); Model C enforces displacement coincidence at tops of the supporting structure. To illustrate the difference in stiffness of the lower support structure at each pipe truss support, unit forces were applied in three directions at each support. The support numbers are illustrated in Fig. 15. The nodal displacements are used to determine the support stiffness, which is listed in Table 16.

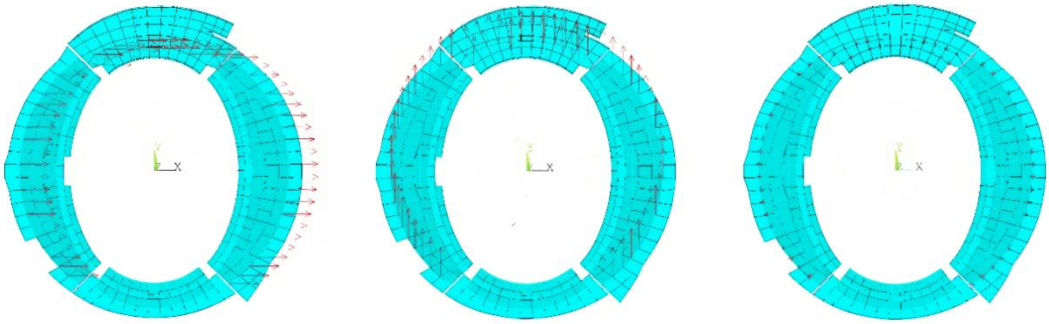

(a) X-direction (b) Y-direction (c) Z-direction

Fig. 15 Apply unit force to lower support structure model

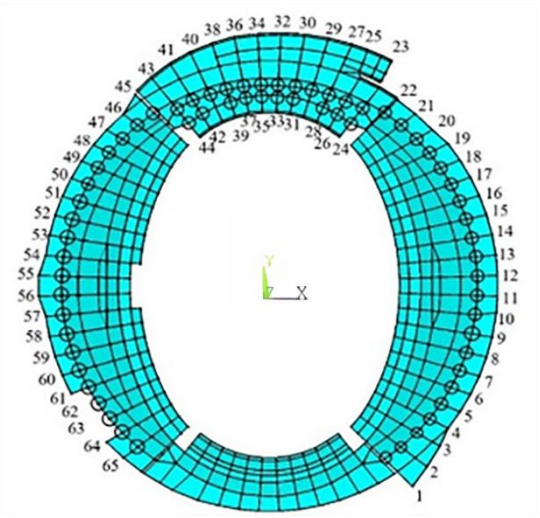

Fig. 16 Location of support columns and corresponding numbers

Table 16
Three- direction stiffness of 65 supports of steel canopy structure (1 x 105kN/m)

Support Number	X-direction	Y-direction	Z-direction	Support Number	X-direction	Y-direction	Z-direction
1	0.99	1.56	1.65	34	1.31	0.54	5.87
2	1.13	1.57	1.84	35	1.33	0.54	7.51
3	1.06	1.43	1.08	36	1.30	0.54	5.87
4	1.12	1.42	1.09	37	1.33	0.54	7.33
5	1.26	1.43	1.34	38	1.31	0.54	6.20
6	1.36	1.44	1.46	39	1.33	0.54	8.81
7	1.45	1.44	1.58	40	1.31	0.53	6.42
8	1.50	1.43	1.59	41	1.32	0.52	6.25
9	1.56	1.43	1.65	42	1.36	0.53	9.11
10	1.65	1.43	1.75	43	1.33	0.51	6.12
11	1.68	1.44	1.79	44	1.39	0.52	8.26
12	1.68	1.44	1.79	45	2.28	5.58	3.86
13	1.64	1.43	1.75	46	2.76	5.74	4.58

14	1.56	1.43	1.65	47	2.75	5.13	3.23
15	1.49	1.43	1.59	48	2.94	5.10	3.51
16	1.45	1.44	1.58	49	3.29	5.15	4.31
17	1.35	1.44	1.46	50	3.53	5.13	4.71
18	1.24	1.43	1.33	51	3.74	5.12	5.21
19	1.11	1.42	1.09	52	3.81	5.06	5.34
20	1.05	1.43	1.07	53	3.95	5.02	5.59
21	1.11	1.57	1.82	54	4.11	5.01	5.80
22	0.98	1.57	1.64	55	4.19	5.02	5.93
23	1.32	0.51	6.05	56	4.20	5.02	5.90
24	1.38	0.52	8.40	57	4.15	5.01	5.86
25	1.31	0.52	5.89	58	4.00	4.99	5.62
26	1.35	0.53	7.65	59	3.75	5.01	5.24
27	1.31	0.53	6.28	60	3.86	5.12	5.24
28	1.34	0.53	8.92	61	3.69	5.13	4.81
29	1.31	0.54	6.50	62	3.47	5.15	4.22
30	1.31	0.54	6.22	63	3.28	5.22	3.71
31	1.33	0.54	8.66	64	3.03	5.25	2.90
32	1.31	0.54	5.88	65	3.15	6.02	3.21
33	1.33	0.55	7.28	-	-	-	-

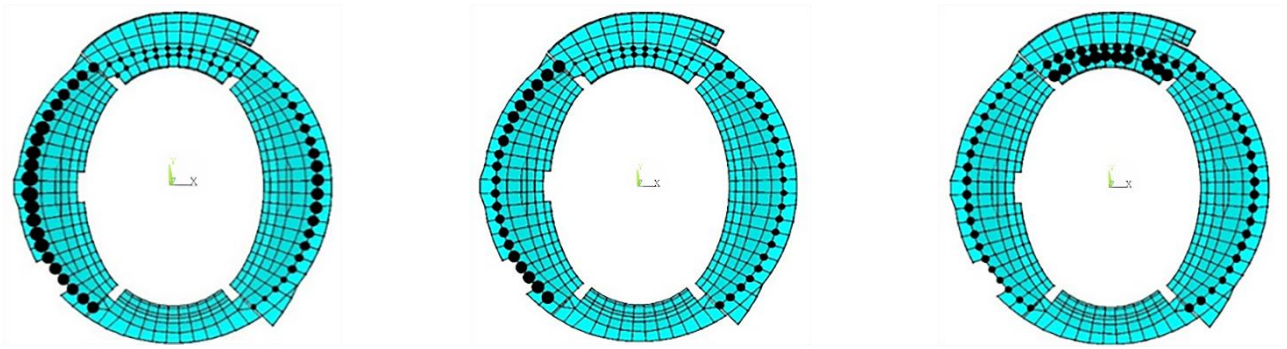

(a) X-direction (b) Y-direction (c) Z-direction

Fig. 17 Three- direction stiffness distribution at the support

To visually show the three-direction stiffness distribution at the support, the stiffness distribution was plotted in Fig. 17. Solid black circles denote support locations, with their areas scaled proportionally to the relative stiffness magnitude. The distribution of stiffness in X, Y and Z directions are shown in Fig. 17 (a), (b) and (c).

As shown in Fig. 17:

1) In the middle part of the east and west sides, the supporting columns of the trusses with the enormous cantilever spans have higher stiffness in the X-direction, while the stiffness shows a decreasing trend toward the columns at two ends..

2) In the middle part of the east and west sides, the supporting columns of the trusses with the smaller cantilever spans have higher stiffness in the Y-direction, while the stiffness shows a decreasing trend toward the columns in the middle.

3) The mid-span columns of east/west sides and the north side support columns have higher Z-direction stiffness.

Given the significant three-directional stiffness differences in lower support columns, the analytical models diverge fundamentally in their boundary assumptions: model B assumes infinite support stiffness; model C considers the displacements at the top of the support as consistent. Both dynamic responses differ from the integrated analytical model A.

To quantitatively assess stiffness inhomogeneity effects, displacement data from 10 radial truss bays are extracted and compared with the field-measured values during canopy construction. Since the measurement points are arranged symmetrically, there are four measurement points (2 cantilever measurement points V1 and two support measurement points V2) for each joint, as shown in Fig. 7. Cantilever nodes displacements are presented in Table 17, while support nodes displacements are detailed in Table 18. Field-measured versus analytical values are comparatively visualized in Fig. 18.

From Table 17, it can be seen that the measured maximum displacement of the cantilever point is -50.0 mm, which is 1/7200 of the span and satisfies the requirement [49-50]. Compared with the finite element analysis value, the maximum error is 29.73%, showing reasonable agreement. From Table 18, it can be seen that the measured value of the node at the support is -16.0mm. Compared with the finite element analysis value, the maximum error is 59.50%. The significantly larger relative error is mainly due to the small absolute displacement magnitudes near supports.

Table 17
Comparison of measured Z-direction displacement of radial truss cantilever point (V1) with finite element value (mm)

Axis line number	Truss number	Field-measured value u_1	Analytical value u_2	Error (%) $(u_2-u_1)/u_1$
S-54	ZHJ-1	-31.00	-32.57	5.06
		-31.00	-33.36	7.61
S-48	ZHJ-7	-38.00	-42.17	10.97
		-37.00	-43.81	18.41

S-45	ZHJ-10	-29.00	-34.64	19.45
		-32.00	-34.06	6.44
S-42	ZHJ-13	-40.00	-43.27	8.18
		-42.00	-45.76	8.95
S-39	ZHJ-16	-45.00	-47.33	5.18
		-43.00	-44.69	3.93
S-33	ZHJ-22	-11.00	-14.27	29.73
		-11.00	-13.42	22.00
S-20	ZHJ-35	-9.00	-11.04	22.67
		-12.00	-13.47	12.25
S-14	ZHJ-41	-35.00	-41.97	19.91
		-41.00	-40.35	-1.59
S-8	ZHJ-47	-41.00	-45.61	11.24
		-46.00	-44.30	-3.70
S-2	ZHJ-53	-50.00	-44.77	-10.46
		-46.00	-43.36	-5.74

Table 18
Comparison of measured Z-direction displacement of node (V2) at radial truss support with finite element value (mm)

Axis line number	Truss number	Field-measured value u_1	Analytical value u_2	Error（%） $(u_2-u_1)/u_1$
S-54	ZHJ-1	-9.00	-6.05	-32.78
		-12.00	-8.71	-27.42
S-48	ZHJ-7	-6.00	-5.26	-12.33
		-4.00	-5.43	35.75
S-45	ZHJ-10	-5.00	-6.73	34.60
		-3.00	-4.28	42.67
S-42	ZHJ-13	-4.00	-5.14	28.50
		-6.00	-6.86	14.33
S-39	ZHJ-16	2.00	2.34	17.00
		-2.00	-3.19	59.50
S-33	ZHJ-22	-1.00	-1.13	13.00
		-2.00	-2.6	30.00
S-20	ZHJ-35	1.00	1.13	13.00
		-1.00	-1.27	27.00
S-14	ZHJ-41	-7.00	-9.05	29.29
		-15.00	-9.62	-35.87
S-8	ZHJ-47	-16.00	-10.27	-35.81
		-13.00	-10.47	-19.46
S-2	ZHJ-53	-12.00	-8.39	-30.08
		-13.00	-8.51	-34.54

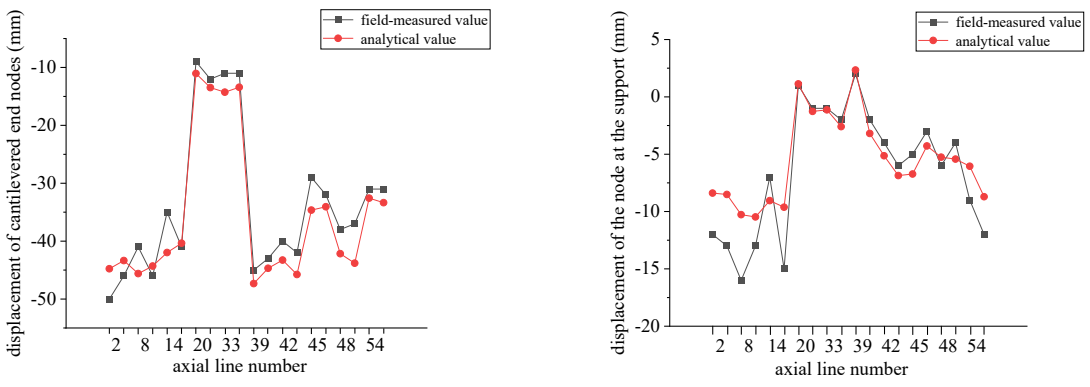

(a) Vertical displacement of cantilever end nodes

(b) Vertical displacement of the node at the support

Fig. 18 Comparison of measured values of displacement of some nodes with FEA values

From Fig. 18, the measured values of displacement and the simulated values from the finite element analysis are basically consistent, indicating that the results of the finite element model analysis are in good agreement with the actual engineering. It verifies the feasibility of the dynamic analysis of the finite

element model presented in this paper and enhances the discussion of stiffness in-homogeneity.

5.2. Acceleration amplification effect

During transmission, ground motion is influenced by factors such as site conditions and the lower structure. To quantify acceleration amplification during energy transfer from lower supports to the steel canopy, seven ground motions are applied to the lower support structure of Model A and Model C. The three-direction output acceleration time histories for each support column top are extracted to obtain the average acceleration response time history curve. For a peak acceleration of 100 gal in the main direction, Table 19 and 20 show the peak ground input acceleration (PGA), peak response frequency acceleration of the supporting columns (PRFA), and acceleration dynamic force amplification factor (DFA) for Model A and Model C, respectively.

It can be seen from Table 19 that, the average values of DAF in the X, Y, and Z directions are 2.05, 2.15 and 1.28, respectively. It indicates that the acceleration amplification effect of the lower support structure in model A is larger in the horizontal X and Y directions but more negligible in the Z direction.

It can be seen from Table 20 that, the average values of DAF in the X, Y, and Z directions are 2.34, 2.08 and 2.25, respectively. It indicates that the acceleration amplification effect of the lower support structure in Model C is larger in three-directions. The amplification factor comparison of the three-direction acceleration for model A and C is shown in Fig. 19.

Table 19
Acceleration amplification effect of the support column obtained from model A calculations

Ground motion	Incentive direction								
	X			Y			Z		
	PGA (gal)	PRFA (gal)	DAF	PGA (gal)	PRFA (gal)	DAF	PGA (gal)	PRFA (gal)	DAF
EL Centro	100	182.88	1.83	85	236.51	2.78	65	77.75	1.20
Northridge	100	239.81	2.40	85	83.51	0.98	65	74.20	1.14
Kobe	100	148.69	1.49	85	247.07	2.91	65	77.61	1.19
Taft	100	206.87	2.07	85	209.53	2.47	65	84.13	1.29
Wo Long	100	260.03	2.60	85	221.65	2.61	65	98.89	1.52
Victoria Mexico	100	174.00	1.74	85	99.33	1.17	65	81.77	1.26
CHICHI	100	221.19	2.21	85	179.31	2.11	65	87.28	1.34

Table 20
Acceleration amplification effect of the support column obtained from Model C calculations

Ground motion	Incentive direction								
	X			Y			Z		
	PGA (gal)	PRFA (gal)	DAF	PGA (gal)	PRFA (gal)	DAF	PGA (gal)	PRFA (gal)	DAF
EL Centro	100	265.96	2.66	85	190.38	2.24	65	167.01	2.57
Northridge	100	265.77	2.66	85	86.51	1.02	65	128.26	1.97
Kobe	100	157.96	1.58	85	302.20	3.56	65	129.83	2.00
Taft	100	266.93	2.67	85	183.46	2.16	65	167.32	2.57
Wo Long	100	246.80	2.47	85	196.72	2.31	65	146.13	2.25
Victoria Mexico	100	182.20	1.82	85	126.00	1.48	65	128.49	1.98
CHICHI	100	250.99	2.51	85	152.66	1.80	65	156.70	2.41

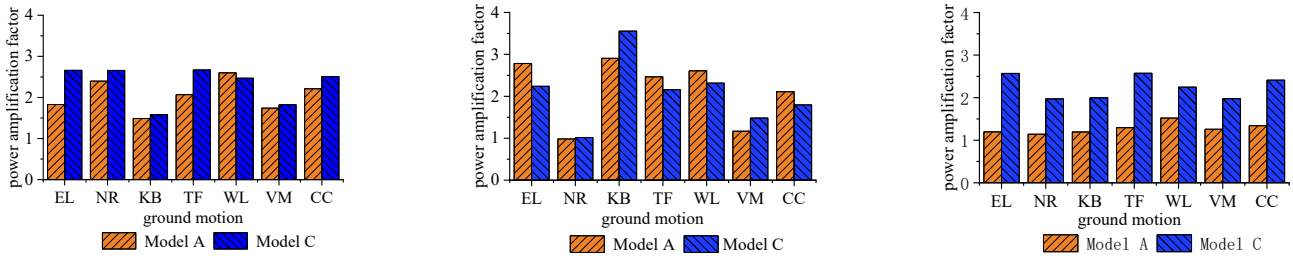

(a) X-direction (b) Y-direction (c) Z-direction

Fig. 19 Amplification factor of the Three-direction

As observed in Fig. 19:

1) For Model A, Northridge and Wolong ground motions amplify X-direction acceleration more significantly, whereas El Centro and Kobe motions amplify Y-direction acceleration more significantly.

2) For Model C, Kobe motion amplifies Y-direction acceleration most prominently.

3) The effect of ground motion on the amplification effect of Z-direction acceleration is similar for both models.

Data from Tables. 19, 20 and Fig. 19 further indicate:

1) The average values of the power amplification factor in the horizontal direction of Models A and C are relatively close.

2) Model C's vertical acceleration dynamic amplification factor is nearly twice as much as that of model A. This discrepancy occurs because model A's integrated steel canopy functions as a three-dimensional metal damper, providing greater horizontal stiffness but lower Z-direction stiffness, thereby enhancing Z-direction damping effectiveness..

Consequently, the lower support structure induces significant three-directional acceleration amplification in both models, with Model C exhibiting approximately twice the Z-direction amplification of Model A. Therefore, when designing the upper steel canopy structure, model B, which does not consider the lower support structure, and model C, which separates the upper and the lower structures, exhibit dynamic response differences compared to the integrated model A. It indicates that the different models exhibit varying dynamic responses.

5.3. Filtering effects

The selective permeability of structures to ground motion leads to significant differences in the effects of ground motion on structures across different frequency bands. The Fourier transform of the ground input acceleration time history and the output acceleration time history at the top of the support column was performed by the Seism Signal software to obtain the principal frequencies of the acceleration time history. The filtering effects of Model A and C for supporting columns under different ground motions are included in Table 21. In this Table, IPF is the principal frequency of the input acceleration time history, and OPF is the principal frequency of the output acceleration time history.

Table 21
Filtering effects (Hz) of supporting columns calculated by Models A and C

Ground motion	Direction of vibration								
	X			Y			Z		
	IPF	OPF (A)	OPF (C)	IPF	OPF (A)	OPF (C)	IPF	OPF (A)	OPF (C)
EL Centro	2.37	3.75	3.10	1.47	4.38	2.08	8.42	4.38	3.10
Northridge	1.07	3.33	3.33	3.22	4.33	1.47	6.98	7.00	3.00
Kobe	0.29	2.00	2.07	2.00	4.27	2.07	2.15	2.20	4.67
Taft	1.42	3.35	2.85	2.98	4.65	2.35	4.40	4.40	4.40
Wo Long	2.34	3.94	3.11	5.47	4.33	2.33	5.91	5.94	3.11
Victoria Mexico	0.98	4.10	3.00	1.76	4.65	2.05	4.64	6.55	4.65
CHICHI	1.47	3.21	3.21	2.54	4.54	2.00	0.49	0.50	3.21
Average value	1.42	3.38	2.95	2.78	4.45	2.05	4.67	4.42	3.73

As can be seen from Table 21:

1) The output average principal frequency OPE of the model A support column in both X and Y directions is larger than the input ground motion principal frequency. At the same time, it is smaller in the Z direction.

2) The output average principal frequency OPE of the model C support columns in the Y and Z directions is smaller than the principal frequency of the input ground motion, except in the X direction.

The lower support structures of models A and C both have some filtering effect on the principal frequency of ground motion. The ratio of the output principal frequency to the input principal frequency for Model A and Model C under seven ground motions is plotted in Fig. 20, showing the difference in filtering effects between the two models.

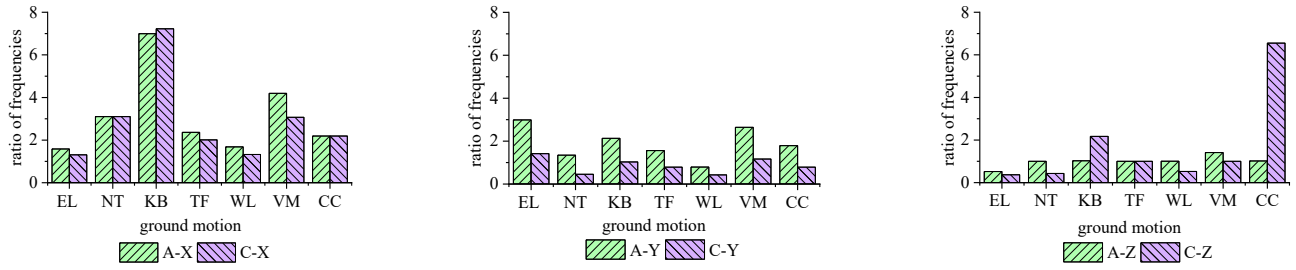

(a) X-direction (b) Y-direction (c) Z-direction

Fig. 20 Filtering effect of lower support structure

As observed in Fig. 20:

1) Due to greater X-direction stiffness in both models' lower support structures, their filtering effects exhibit closer alignment in this direction.

2) In the Y-direction, model A demonstrates higher output-to-input principal frequency ratios than model C, indicating distinct filtering behavior.

3) In the Z-direction, the filtering effect of model C on Kobe and CHICHI ground motions is significantly different from that of model A.

The above analysis indicates a difference in the filtering effects between Model A and Model C. In particular, the Z-direction will influence the principal frequency of ground motion input to the steel canopy structure, which in turn will affect its dynamic response.

These frequency shifts have potentially significant implications for the safety performance of the steel canopy structure, primarily manifested in two damage mechanisms:

1) Resonance Amplification Risks

When the dominant frequency of filtered ground motions shifts close to the natural frequency of key areas in the steel canopy (e.g., cantilever tips), it can excite significant resonance effects. Classical theories indicate [53] that such frequency-domain overlap can lead to the doubling of acceleration and displacement responses, triggering two typical failures:

a) Main structure instability: Amplified inertial forces cause inelastic buckling of compression chords in pipe trusses or brittle shear failure of support anchor bolts [54].

b) Secondary system cascading failure: Excessive support displacements may cause buckling-restrained braces to lose energy-dissipating capacity [55].

2) High-Frequency Fatigue Accumulation

Filtering effects also alter the high-frequency energy distribution of ground motions. Engineering practice confirms that although such high-frequency vibrations do not cause immediate failure, they induce cumulative damage through repeated stress cycles [56], leading to:

a) Joint fatigue cracking: Cyclic stresses concentrated at tubular joint welds initiate micro-cracks, which eventually propagate through the pipe wall [57].

b) Connection functional degradation: High-frequency micro-vibrations cause continuous loosening of metal roof panel bolts, weakening the airtightness and wind resistance of the envelope system.

These mechanisms demonstrate that differences in Z-direction filtering effects between Model A and Model C directly influence the canopy's damage modes. The excessive low-frequency shift in Model C may underestimate resonance risks at cantilever tips, necessitating verification of the true filtered spectrum using the integrated Model A.

6. Conclusions

In this study, the seismic performance of a large stadium steel canopy structure was researched, and the following conclusions were obtained:

1) The results of stress and displacement calculations for integrated model A are intermediate between the two simplified models: model B and model C. To reduce computational resources, the seismic calculation results of simplified models B and C can be used as upper and lower reference values during the preliminary design of the structure.

2) A simplified calculation method is proposed, which can approximate the structural response of the integrated model based on the simplified model calculated data. Simplified calculations of stresses and displacements can be provided for the seismic analysis of the steel canopy structure during the preliminary design stage.

3) The vertical damping filtering effect of the upper steel canopy structure

resulted in a closer vertical acceleration amplification factor of model A and model C. The difference in the vertical acceleration amplification effect is obvious.

4) Comparison of the output average acceleration time history principal frequencies at the top of the lower support structure for Model A and Model C reveals that the filtering effect of the lower support structure is not negligible. An integrated model should be used for accurate calculations.

5) The integrated shape of the lower support structure is like that of a saddle. In the north-south direction, the steel canopy structure is presented as a relatively uniform frame structure. On the east-west sides, it is expressed as a diagonal cantilever structure with disparate scales. This design resulted in substantial differences in the three-direction stiffness at the top of the supporting columns and an uneven distribution of the integrated structural stiffness, which is the main reason for the large differences in the dynamic response of the three models. Integrated analysis is therefore essential for seismic design of large cantilevered steel canopies.

Acknowledgements

This work was financially supported by the Natural Science Foundation of Anhui Province, China (21080850E252) and the Anhui Province Housing and Urban Rural Construction Science and Technology Plan Project(2022-YFO89).

References

[1] Chen W, Chan T.M. Seismic design and parametric study of steel modular frames with distributed seismic resistance. Thin-Walled Structures, 2023, 182(PB).
[2] Guan B, Su M, Lian M. Seismic behavior of combined steel framed tube the lower support structure with replaceable shear links. Journal of Constructional Steel Research, 2020, 167105968-105968.
[3] Zhang A, Fang H, Liu X, et al. Seismic response analysis of large-span steel structures in zone C5 of the terminal building of Beijing Daxing International Airport. Advances in Architectural Steel Structures, 2021, 23(01): 25-30. (in Chinese)
[4] Zhang A, Wang X, Liu X, et al. Study on shaking Tab. test of large-span steel structure of terminal building of Beijing Daxing International Airport with integrated model of scaling. Journal of Building Structures, 2021, 42(03): 1-13. (in Chinese)
[5] Liang C, Zhu Z, Qin K, et al. Research on seismic design of roof steel structure of Beijing new airport terminal building. Steel Structure, 2020, 35(05): 19-26. (in Chinese)
[6] Lu B, Gong J. Seismic response analysis of large-span tensile truss structures under rare earthquakes. Steel Structure, 2019, 34(11): 50-55. (in Chinese)
[7] Xiao W, Wang J, Wan L, et al. Structural analysis of a multi-story steel exhibition hall. Building Structure, 2021, 51(15): 38-43. (in Chinese)
[8] Tong J. Study on seismic performance and ultimate bearing capacity of a shaped multi-tower linked high-rise structure under megathrust earthquake. Building Structure, 2020, 50(13): 101-105. (in Chinese)
[9] Wang D, Wang L, Xu J, et al. A directionally-dependent evolutionary lagged coherency model of nonstationary horizontal spatially variable seismic ground motions for engineering purposes. Soil Dynamics and Earthquake Engineering, 2019, 11758-71.
[10] Jian S, Kaiming B, Kun X, et al. Influence of spatially varying ground motions on the seismic responses of adjacent bridges coupled by a tuned inerter damper. Soil Dynamics and Earthquake Engineering, 2022, 154.
[11] Rodda K. G, Basu D. Spatially correlated vertical ground motion for seismic design. Engineering Structures, 2020, 206(C): 110191-110191.
[12] Bi K, Hao H, Ren W. Response of a frame structure on a canyon site to spatially varying ground motions. Structural Engineering and Mechanics, 2010, 36(1): 111-127.
[13] Hao H and Duan X, Multiple excitation effects on response of symmetric buildings. Engineering Structures, 1996,18(9): 732-740.
[14] Watson-Lamprey J, Abrahamson N. Selection of ground motion time series and limits on scaling. Soil dynamics and earthquake engineering, 2006, 26(5): 477-482.
[15] Katsanos I. E, Sextos G A, Manolis D G. Selection of earthquake ground motion records: A state-of-the-art review from a structural engineering perspective. Soil Dynamics and Earthquake Engineering, 2009, 30(4): 157-169.
[16] Ao D, E J.P. Refined multivariate return period-based ground motion selection and implications for seismic risk assessment. Structural Safety, 2021, 91.
[17] Bradley A B. A ground motion selection algorithm based on the generalized conditional intensity measure approach. Soil Dynamics and Earthquake Engineering, 2012, 4048-61.
[18] Wang G. A ground motion selection and modification method capturing response spectrum characteristics and variability of scenario earthquakes. Soil dynamics and earthquake engineering, 2011, 31(4): 611-625.
[19] Sinković L N, Dolšek M, Žižmond J. Impact of the type of the target response spectrum for ground motion selection and of the number of ground motions on the pushover-based seismic performance assessment of buildings. Engineering Structures, 2018, 175731-742.
[20] Kowsari M, Halldorsson B, Hrafnkelsson B, et al. Selection of earthquake ground motion models using the deviance information criterion. Soil Dynamics and Earthquake Engineering, 2019, 117288-299.
[21] Eftekhari N, Yazdani A, Razmyan S, et al. Data envelopment analysis based procedure for selection and ranking of ground motion prediction equations[J].Soil Dynamics and Earthquake Engineering, 2020, 137.
[22] Gao J, Yao J, Chen L, and Cheng Z. Optimized scheme for ground motion selection based on fuzzy synthesis decision-making. Soil Dynamics and Earthquake Engineering, 2021, 18: 106580.
[23] Dai J, Chen J, Zhang C, et al. Seismic Damage Investigation and Seismic Performance Study of Lushan Middle School Gymnasium. Journal of Performance of Constructed Facilities, 2020, 34(3).
[24] Xue S, Liu Y, Li X, et al. Current status and prospect of research on cooperative work problems of large-span spatial structures. Industrial Building, 2015, 45(01): 1-9.
[25] Nie G. On the buckling of imperfect squarely-reticulated shallow spherical shells supported by elastic media. Thin-Walled Structures, 2003, 41(1): 1-13.
[26] Nie G,Wang W,Du K,et al. A review on the development of seismic theory for large-span spatial structures. World Earthquake Engineering, 2020, 36(02): 21-34. (in Chinese)
[27] Nie G, Zhi X, Shang Y, et al. Study on seismic performance of single-story column-faced mesh shell structure considering lower support effect. Journal of Building Structures, 2020, 41(S1): 10-16. (in Chinese)
[28] Wang Y, Jiang J. Research on the effect of concrete support on the mechanical performance of large-span spatial lattice structures and simplified analysis method. Building Structure, 2019, 49(09): 43-47. (in Chinese)
[29] Yu Z, Zhi X, Fan F, et al. Effect of the lower support structures upon failure behavior of steel reticulated domes subjected to the severe earthquake. Thin-Walled Structures, 2011, 49(9):1160-1170.
[30] Zheng Y, Wang R.Q, et al. Dynamic analysis of anti-dip bedding rock slopes reinforced by pre-stressed cables using discrete element method. Engineering Analysis with Boundary Elements, 2021.
[31] Meng J.X. Comparative Analysis of Space Truss Door Beams Based on Different Calculation Models. Research on Engineering Technology, 2023,8(15): 106-108.（in Chinese）
[32] Xia W.J. Electrochemical Seismic Design and Artificial Intelligence System Modeling of High-Rise Steel Structure Buildings. Journal of Chemistry, 2022.
[33] Han Q.H, Sun M.Y. et al. Ground motion parameters and fragility analysis for single-layer reticulated domes supported by the lower support structures. Earthquake Engineering and Engineering Vibration, 2024, 44(03): 29-40.（in Chinese）
[34] Chopra, A.K. Naeim F. Dynamics of Structures—Theory and Applications to Earthquake Engineering, Third Edition. Earthquake Spectra, 2007, 23(2): 491-492.
[35] M. Birchall. 22-Recent developments in architectural fabric structures in Europe: The des--ign and construction of the London 2012 Olympic Stadium and its context in the European fabric structures market. Fabric Structures in Architecture, 773-817, 2015.
[36] Zhang S, Liu N, Li W and Yan S. Umbrella structure building design method via case-based design and statistical analysis of structural morphological parameters, Journal of Building Engineering, 2022, 45: 103542.
[37] Fan C, Yang K, et al. Design and research on large-span roof structure supported by mega arches of Xiamen Egret stadium. Journal of Building Structures, 2023, 44(09): 27-39.（in Chinese）
[38] Ivan B, Alen H, Vesna J.P. Conceptual design of arena Nikola gazdic stadium split. Proceedings of the Faculty of Civil Engineering, 2019, 9(18): 28-37.
[39] Seismic Design Criteria for Structures, Systems and Components in Nuclear Facilities. ASCE/SEI Standard 43-05, American Society of Civil Engineers (ASCE), Reston, Virginia. 2016.
[40] Guyan R J. Reduction of stiffness and mass matrices. AIAA Journal, 1965, 3(2): 380.
[41] NERHP recommended seismic provisions for new buildings and other structures. FEMA P-750 report prepared by the Building Seismic Safety Council of The National Institute of Building Sciences for the Federal Emergency Management Agency, Washington, D.C; 2009.
[42] Ferrante A, Dubois F, Morenon P. Comparison of Continuous and Discrete Modeling Strategies for the Structural Assessment of a Masonry Vault Under Dynamic Seismic Loading. International Journal of Architectural Heritage, 2024, 18(12): 1873-1885.
[43]Code for Seismic Design of Buildings, GB 50011-2010, China Academy of Building Research, Institute of Engineering Mechanics, China Earthquake Administration, China Architectural Design and Research Group, China National Institute of Standards and Design for Buildings, Beijing Institute of Architectural Design, 2010.
[44] Engineers C O S A. Minimum Design Loads and Associated Criteria for Buildings and Other Structures. American Society of Civil Engineers, 2022.
[45] Lignos G D, Krawinkler H, Whittaker S A. Prediction and validation of sidesway collapse of two scale models of a 4-story steel moment frame. Earthquake Engineering & Structural Dynamics, 2011, 40(7): 807-825.
[46] Kunnath K S, Nghiem Q, El-Tawil S. Modeling and Response Prediction in Performance-Based Seismic Evaluation: Case Studies of Instrumented Steel Moment-Frame Buildings. Earthquake Spectra,2004,20(3):883-915.
[47] Pujari N. N, Ghosh S, Lala S. Bayesian Approach for the Seismic Fragility Estimation of a Containment Shell Based on the Formation of Through-Wall Cracks. ASCE-ASME Journal of Risk and Uncertainty in Engineering Systems, Part A: Civil Engineering, 2015, 2(3).
[48] Zhang C.X. Study on the Failure Mechanism under Strong Earthquake Excitation and Isolation of Space Double-layer Lattice Structure. Institute of Engineering Mechanics, China Earthquake Administration, 2016. (in Chinese)
[49] Standard for acceptance of construction quality of steel structures: GB 50205-2020. China Planning Press, 2020.
[50] Design of steel structures: GB 50017—2017. China Planning Press, 2017.
[51] High strength low alloy structural steels: GB/T 1591-2018. Standards Press of China, 2018.
[52] Rubber bearings—Part 3: Elastomeric seismic-protection isolators for buildings: GB/T 20688.3-2006. Standards Press of China, 2006.
[53] Liu Z, Chen J. Structural dynamics. China Water&Power Press:2012.
[54] ELNASHAI A, SARNO D.L. Earthquake Engineering: From Engineering Seismology to Performance-Based Engineering, Journal of Earthquake Engineering, 2004, 8(6): 963-964.
[55] Kitayama S, Constantinou C.M. Seismic Performance of Buildings with Viscous Damping Systems Designed by the Procedures of ASCE/SEI 7-16. Journal of Structural Engineering, 2018, 144(6).
[56] Cui D, Xie R, Li M, et al. Time-dependent reliability analysis for structures under multilevel loads based on fatigue damage theory. Engineering Failure Analysis, 2024.
[57] Hobbacher F A. The IIW fatigue design recommendations - newly revised and expanded. Welding in the World: Journal of the International Institute of Welding: Journal of the International Institute of Welding, 2007, 51(Suppl.1): 243-254.